Laser-filament-induced condensation in sub-saturated environments

Mémoire

Aravindan Sridharan

Maîtrise en Physique
Maître ès sciences (M.Sc.)

Québec, Canada

Résumé

En ce qui concerne des méthodes d'ensemencement de nuages, les filaments de laser ont des avantages particuliers par rapport à des méthodes traditionnelles. Jusqu'à présent, la condensation induite par le filament de laser a été observée uniquement dans des conditions saturées ou sursaturées. La condensation induite par le filament dans des conditions sous-saturées reste un domaine presqu'inconnu. Nous postulons que la condensation est possible dans des conditions sous-saturées dans la mesure où la cadence des impulsions femtosecondes soit élevé, et qu'une cadence élevée pourrait engendrer une turbulence plus forte, ce qui contribuerait à la condensation. Pour mieux comprendre la condensation dans une condition sous-saturée, nous utilisons une chambre à nuages inversée. Nos recherches permettent d'observer la présence d'agrégats de brume à l'œil nu ainsi qu'au moyen d'une caméra numérique, et la croissance des gouttelettes d'eau en dessous du filament, ce qui confirme notre hypothèse.

Abstract

Laser filaments have unique advantages compared to other traditional methods when it comes to cloud seeding techniques. Till now, laser filament induced condensation has been observed in saturated or super-saturated conditions alone. Filament induced condensation in sub-saturated conditions remains mostly unexplored. We postulate that condensation is possible in sub-saturated conditions if femtosecond laser pulses of high repetition rate capable of generating a turbulence strong enough to contribute to the condensation process are used. To better understand condensation in sub-saturated conditions, an inverted cloud chamber is used. In our findings, we observe mist packets with and without a digital camera, as well as growth of water droplets under the filament, which in turn confirm our hypothesis.

Contents

List of Tables

List of Figures

List of Acronyms and Abbreviations

AOM Acousto-optic modulator

CCN Cloud Condensation Nuclei

COPL Centre for Optics, Photonics and Lasers

CPA Chirped Pulse Amplification

CW Continuously Working (viz. CW Laser)

E. R. H Equilibrium Relative humidity

REGEN Regenerative amplifier

R. H Relative humidity

SIOM Shanghai Institute of Optics and fine Mechanics

SPM Self-phase modulation

To Mom and Dad,

you have been the fountain of

inspiration.

ஊக்கத்தின் ஊற்றாக

திகழ்ந்தயென் பெற்றொர்க்கு

இவ்வாராய்ச்சிக்கட்டுரையை

சமர்ப்பிக்கிறேன்

Acknowledgements

गुरुर्ब्रह्मागुरुर्विष्णुर्गुरुर्देवोमहेश्वरः।
गुरुरेवपरंब्रह्मतस्मैश्रीगुरवेनमः॥
(गुरुमन्त्र)

The Teacher is the creator,
the sustainer, and the reformer;
He is verily the supreme being,
salutations to that Teacher.
(Guru Mantra)

The mantra above in Sanskrit is the first maxim taught to students in India, for it stresses the importance of the teacher, or the guru, in shaping the life of the student. At the beginning of any auspicious work, especially intellectual in nature, it is customary in Indian tradition to pay respects to the guru. In my case, my guru, Professor See Leang Chin, invited me with arms wide open to work in his group when I was just a sophomore in Engineering Physics. Not only has he been a noteworthy director who has been the fulcrum of my Masters dissertation, but also an excellent role model. I am deeply indebted to his words of wisdom and encouragement. The lessons that have been learnt from our countless interactions will forever remain etched in my mind.

My heartfelt thanks go to my professors who have generously accepted to evaluate this dissertation, namely Prof. Michel Piché and Prof. Bernd Witzel. Prof. Piché never showed the slightest hesitation to share his valuable knowledge and experience with his students. It has been an enriching experience to learn from him and to have rubbed shoulders with a living laser encyclopedia, as he is rightly called. I have also had the good fortune to attend the courses of Prof. Bernd Witzel. The discussions had in class rife with the enthusiasm characteristic of Prof. Witzel have immensely contributed my research work.

I would like to thank my colleagues, Tie-Jun Wang, Jingjing Ju, Ali Azarm, Feng Liang, Sima Hosseini, and Shuai Yuan for all the support I have received from them. Most of the experiments that are presented in this dissertation have been done with Tie-Jun and Jingjing. Tie-Jun has participated in most of the experiments and has always been very patient with me from the time I was a beginner in laser alignment. As for working with Jingjing, it has always been unforgettable mix of work and play. She has been very generous in her suggestions and ideas vis-à-vis this dissertation. An important member of our group to whom I am very grateful is our technician Mario Martin, who has been instrumental in the construction of the whole experimental setup. Last but not least, I would like to convey my sincere thanks to Sharan Kumar Subramanian, doctoral student of Indian Linguistics, who helped me with the painstaking task of proof-reading this dissertation.

Foreword

This dissertation is written to conclude the research oriented masters program in physics at Université Laval. The experiments were conducted at the Center for Optics, Photonics, and Lasers (COPL) under the guidance of professor See Leang Chin. There are three main sections in this dissertation which are the nitrate adsorption experiment, the droplet measurement experiment and the turbulence analysis. At the final stages of this dissertation, the first two sections were published in *Laser Physics Letters* under the title "Laser-filament-induced condensation in an inverted cloud chamber" and the last section was published in *Physics Review E* under the title "Laser-filament-induced snow formation in a subsaturated zone in a cloud chamber: Experimental and theoretical study".

I was the principal investigator for the experiments presented in the first two sections. These experiments were carried out with the extensive support of my colleagues Tie-Jun Wang and Shuai Yuan. The lead researcher for the experiments presented in the last section is Jingjing Ju, another co-researcher. I participated in those experiments, for which the results are presented here to give a complete understanding of the laser-induced condensation phenomena observed in our laboratory at Université Laval. As the author, I grant the rights to use in part or in whole, the contents of this dissertation to my professor See Leang Chin and my colleague Jingjing Ju. This work is the result of a long-lasting collaboration between our institute and the Shanghai institute of Optics and Fine Mechanics (SIOM).

Introduction

In the recent past, there has been a great number of interesting advancements in the field of laser filament induced condensation in air. Filamentation [1–13] is a phenomenon that can be observed when the duration of the laser pulse is very short, specifically in the range of ten to hundred femtoseconds (1 fs $= 10^{-15}$ s). In a homogeneous medium such as air, the beam, through non-linear processes, will self-focus [14–17] and will give rise to a narrow long column of weakly ionized plasma ($\sim 10^{16}$ cm^{-3}) [18–22] called filament. Various models have been put forth in order to explain the process of filamentation, namely the moving focus model [23], the self-guiding model [24], the dynamic spatial replenishment model [25], and the spatial solitons and light bullets model [26]. Although most of these models have differences in their estimations of certain parameters, they all share a common ground in the self-focusing and plasma creation aspects of the filament. Filamentation is a fundamental concept in many actual and potential applications such as remote detection of pollutants [27–32], lightning control [33–35], and terahertz generation [36–40], among others. The principal area of interest in this dissertation is femtosecond laser filament initiated water condensation in sub-saturated conditions as found in clouds.

Since time immemorial, man has contemplated on the workings of nature and the effective use of weather conditions to suit his needs. This can be clearly seen in the rain summoning rituals of certain ancient as well as modern cultures. It is well known that climate control could have a significant impact on agriculture and on a plethora of other human activities. The processes leading to condensation and precipitation have already been

thoroughly documented by atmospheric scientists [41, 42]. Their research has shown that dispersion of certain particles like dry ice or salts such as sodium chloride and silver iodide can be used to seed clouds [43]. These techniques are now widely used to regulate climate, but the affordability of such techniques is still hotly debated and hence there is immense scope for alternatives.

One such alternative is laser induced condensation. Initial experiments were done in Japan by Prof. Yoshihara's group at the Toyota Chemical and Physical Research Institute in 2005 [44, 45]. The Teramobile research group from the University of Geneva in Switzerland went one step further by proposing the idea of using a laser filament as a cloud seeding mechanism [46–53]. Filaments offer unique advantages compared to other alternatives. They can be triggered remotely, can provide an interaction zone or seeding volume that could stretch to more than 100 metres, and can propagate through adverse conditions like low pressure, turbulence and fog. To put the idea to test, experiments were carried out and it was shown that condensation could indeed be induced by laser filaments. The results obtained using a diffusion cloud chamber in the laboratory [46, 54–56] were identical to experiments conducted outdoors. Thereafter, more attention has been given to the underlying physical and chemical interactions of this phenomenon. It was observed that processes such as photodissociation, ionisation and electron collision in molecules such as H_2O, O_2, and N_2, could open up new chemical pathways that could lead to the generation of up to $\sim 10^{14}$ molecules/cm^3/s of HNO_3 in air [48]. The generation of HNO_3 is usually followed by the formation H_2O-HNO_3 clusters that eventually transform into cloud condensation nuclei (CCN). The latter are then propelled in the surrounding humid environment, thereby enhancing droplet growth. The Teramobile group has confirmed that it is possible to induce condensation using laser in a sub-saturated condition at values of relative humidity as low as 75% [50].

Similar experiments have been conducted at SIOM (Shanghai Institute of Optics and Fine

Mechanics) [57–59] to verify the model proposed by the Teramobile group. The researchers at SIOM used a setup in which a cold plate with a temperature of $-46\,^{\circ}$C, was placed at the bottom of a cloud chamber. The temperature at the top of the chamber was equivalent to ambient room temperature ($\sim 20\,^{\circ}$C). A water bath was placed at the top of the chamber to produce vapour. The temperature gradient was generated over a vertical distance of about 20 cm. Formation of ice and snow resulting from direct nucleation of H_2O-HNO_3 clusters was observed. The existence of HNO_3 in the snow and ice was confirmed using pH paper and ion chromatography. The modification of the chopping rate of the 1 kHz laser beam opened newer vistas in the field of filament induced condensation. It was found that nucleation in the active filament volume alone was insufficient to sustain efficient droplet/ice/snow formation. In addition, the alterations of the chopping rate also underline the role of turbulence surrounding the filament in the generation of ice and snow. Since turbulence helped propagate the condensation nuclei to zones farther away from the filament where water vapour concentration could be more significant, this lead to even greater condensation.

The first chapter of the dissertation discusses the underlying theories that are necessary to get a good grasp of the experimental procedures and results. This is followed up with a description of the laser system in the second chapter. The third chapter presents the nitrate adsorption measurement carried out to confirm the existence of HNO_3 in sub-saturated environments. The fourth chapter contains a description of an experiment, called droplet growth measurement, used to verify condensation induced by filament in sub-saturated environments. The fifth chapter outlines the results of experiments carried out to understand the effects of filament-induced turbulence in condensation. The conclusion is based on the observations made throughout the five chapters.

In the experiments on laser filament induced condensation heretofore carried out, the cloud chambers were based on a design with a cold plate placed at the bottom. As a consequence, the temperature increased with increasing altitude. Filaments were generated

in saturated or super-saturated zones near the cold plate. But, filament induced condensation in sub-saturated environments found in nature had not yet been explored. We attempt to investigate the laser induced effect under an inverted temperature gradient, meaning a cold zone at the top and warm at the bottom imitating the decreasing temperature with altitudes observed in the natural environment. A commercial thermoelectric cold plate was placed at the top of the chamber to create the inversed gradient. Quantitative comparisons with previous experiments were not possible with the setup mentioned above, in particular, with the experiment conducted at SIOM [57–59]. Many parameters such as the cold plate's minimal operating temperature ($-18\,^{\circ}$C in our case versus $-46\,^{\circ}$C in the SIOM case [57–59]), the laser pulse energy (1.95 mJ versus 9 mJ) and the thermodynamic conditions inside the chamber were different. Most importantly, the laser was fired in a super-saturated zone ($\sim$127% R. H at $-29\,^{\circ}$C), while in our case it is fired in a sub-saturated zone.

The inversed temperature gradient was approached by two sets of experiments. In the first set, nitrate adsorption measurement, only the mass of NO_3^- ions coming from condensation was measured using ion chromatography for samples collected after $\sim$1.5 hours of laser irradiation from a receptacle placed at different distances from the cold plate. The water mass could not be measured due to rapid evaporation of the droplets falling into the receptacle. The ion chromatography results suggested that condensation was induced by laser filaments. In the second experiment, droplet growth measurement, the receptacle was placed on a cold finger in order to preserve the droplets inside. The objective was to get an estimate of the total growth in water droplets inside the receptacle after $\sim$3 hours of laser irradiation, at a distance of $\sim$1 cm from the cold plate. A significant increase in the water mass was detected.

In both the experiments, the turbulence pattern could not be clearly observed using a lens with a focal length of 50 cm placed at the entrance of the chamber of inversed temperature gradient. To understand the effect of turbulence in the sub-saturated condition, a separate experiment was conducted using a normal temperature gradient where the cold plate is placed

at the bottom. The laser was fired at a distance of $\sim$1 cm from the cold plate in a sub-saturated zone (R. H = $\sim$73%, T = $\sim$4.3 °C) and four lenses having focal lengths of 20, 30, 50 and 80 cm were tested to see if any of these lenses could amplify the production of snow on the cold plate. The 20 cm lens produced the largest amount of snow ($\sim$12 mg) and this pile took the shape of an ellipse that was perpendicular to the laser axis. In addition, the strongest and most discernible turbulence pattern that took the shape of a twin vortex was observed for the first time when using the lens having a focal length of 20 cm. A detailed study of the physical mechanism behind the turbulence-induced amplification of water condensation and snow formation is taken up in the fifth chapter.

Research problem

In previous experiments carried out by Teramobile and SIOM, a diffusional cloud chamber with a cold plate on the bottom and water vapour diffusing from the top allowed for the exploration of super-saturated conditions alone. Condensation in sub-saturated conditions such as those present in clouds was largely unexplored.

Hypothesis

We postulate that condensation is possible in sub-saturated environments that are present in clouds, using lasers of high repetition rate capable of producing cloud condensation nuclei and strong turbulence which are important factors in enabling droplet growth.

Chapter 1

Theory

1.1 Physics of filamentation

The process of laser induced filamentation [1–13] was first observed by Braun et al. at the University of Michigan in 1995 [13]. They noticed for the first time, the self-channeling of a high-peak-power femtosecond laser pulse in air. This self-channeling was found to be a result of equilibrium between two processes, namely Kerr self-focusing [14–17] and plasma induced defocusing in the self-focal volume [18–22]. In a homogeneous medium such as air, when the field intensity is sufficiently high, the refractive index can be expressed by an intensity dependent Taylor series.

$$n(I) = n_0 + n_2 I \tag{1.1}$$

In the preceding equation, n_0 is the refractive index in the linear condition, n_2 is the second order non-linear refractive index coefficient and I is the intensity of the incoming laser beam [14]. Normally, in linear optics, it is not possible to observe the Kerr effect. This is not the case in nonlinear optics in which femtosecond laser pulses with high instantaneous peak powers are used. A typical beam of Gaussian spatial distribution will induce a pronounced change in the refractive index at the center of the beam profile causing a longer

optical path for the rays at the center. As a consequence of this self-induced Kerr lens, the beam wave front will curve in the forward direction towards a focal point on the propagation axis. The pulse peak power P_{cr} at which this Kerr lens effect compensates divergence from linear diffraction is defined as follows [16]:

$$P_{cr} = \frac{3.77\lambda^2}{8\pi n_0 n_2} \tag{1.2}$$

Once the peak power exceeds this critical value, the beam will initiate self-focusing. It is well known that the Kerr lens is not like any common lens. In the Kerr lens, the beam profile enters a dynamic accumulative loop, where it undergoes a reduction in size with the initial self-focusing. This will lead to higher intensities, further causing the Kerr lensing to be more pronounced and the loop continues. Ideally, in the absence of obstacles that could limit the looping process, physical or other, the pulse would focus onto to a singular point where all the energy would be concentrated and would collapse [20]. In air, $n_0 \approx 1$ and $n_2 \approx 4 \times 10^{-23}$ m^2/W at $\lambda = 800$ nm. By substituting these values in 1.2, a critical power of $P_{cr} \approx 2.4$ GW can be found for air.

Practically speaking, other non-linear effects such as tunnel ionisation and multiphoton ionization come into play and prevent this collapse. In the multiphoton/tunnel ionization approximation, the ionisation probability depends non-linearly on the intensity. At a central wavelength of $\sim$800 nm, it would take about 8 photons to ionize O_2 and about 10 photons for N_2 at intensities ranging from 10^{12} to 10^{14} W/cm^2 [21]. The fast ionisation creates a channel of low density plasma ($\sim 10^{16}$ cm^{-3}) along the beam axis and the variation in the refractive index of this plasma can be found using the Drude model [22]. The refractive index of the plasma is lower than that of the surrounding air and this will create a defocusing lens effect because the optical path of light inside the plasma is smaller than that of the surrounding medium. Thus, the balancing effect between the Kerr self-focusing and plasma defocusing can be sustained for very long distances, say up to two kilometres [27]. Owing to nonlinear

energy losses from the generation of plasma, there would eventually be an imbalance that would prevent the filament from growing further. An important characteristic of the filament is that the intensity along the propagation axis is said to be clamped. This would mean that the laser beam intensity would not be higher than the bare value required for generating plasma that is dense enough to defocus the beam. In air, the value of the clamped intensity was found to be around 5×10^{13} W/cm^2 [10–12].

Many models have been put forth based on this idea of equilibrium between self-focusing, plasma induced defocusing and linear diffraction. However, the most accepted model is called the slice-by-slice focusing model, also called the moving focus model [23]. In this model, the non-uniform temporal profile is taken as a prime consideration. The Marburger's formula [15] is used to calculate the self-focusing distance Z_f.

$$Z_f = \frac{0.367ka_2^0}{\{[(\frac{P}{P_{cr}})^{\frac{1}{2}} - 0.852] - 0.0219\}^{\frac{1}{2}}} \tag{1.3}$$

In the above equation, k is the wave number, a_0 is the radius of the beam profile at $1/e$ level of the intensity and P, the peak power of the temporal slice. This equation supports the idea that the peak power of the slices influences the self-focusing length of the slice. The length decreases with increasing peak power. The temporal profile can be split into a large number of slices and the slices containing a peak power that is above the self-focusing threshold will self-focus at different points on the propagation axis. The central slice will focus at a distance Z_f from the beginning of the propagation as given by equation 1.3. Going by equation 1.3, the slice in front of the central one will then self-focus at a farther position due to its lower peak power. These slices will undergo self-focusing, intensity clamping, de-focusing and will then return a reduced amount of energy back to background reservoir. This loop will occur for all the successive slices having a peak power higher than the critical power P_{cr} required for self-focusing. Due to this loss in energy, the front part of the pulse

would become thinner as it propagates. As for the slices in the rear, in principle, they would self-focus at positions that are slightly ahead of the self-foci of the frontal slices. But, this does not occur because they enter into contact with the plasma left behind by the previous slices in the front part. Thus, the self-focusing of the slices in the rear part of the pulse gives rise to a complex intensity distribution after the interaction with the plasma [8].

The above mentioned properties of the filament are what make it an interesting tool for cloud seeding. In brief, the dynamic equilibrium between the self-focusing and plasma defocusing gives a long interaction zone that keeps feeding new CCN. The filament can be remotely triggered by controlling the parameters shown in Marburger's equation 1.3. Previous experiments have shown that filaments could be triggered at multi-kilometer range [27]. The properties of the filament allow it to be sustained through foggy, cloudy conditions as well as turbulent conditions. An important trait that has not been discussed here is the thermal or explosive nature of the filament. At a higher repetition rate, the explosive nature can be used to spread the CCN through a sustained turbulence that would further enhance the seeding process and droplet growth.

1.2 The dynamics of laser-induced condensation

The dynamics of laser-induced condensation is still a subject of ongoing research and the big picture is far from complete. In this section, the basics of condensation [41] and a summary of the research done by multiple groups will be presented [44–53, 57–59]. To understand condensation, one needs to refer to the definition of the relative humidity (R. H) in a mixture of water vapour and ambient air. The relative humidity (R. H) is defined as:

$$\text{R. H} = \frac{e}{e_s(T)} \tag{1.4}$$

where e is the partial vapour pressure, $e_s(T)$ is the saturation vapour pressure of water

at a given temperature T. At the saturation point, the relative humidity (R. H) is equal to unity (R. H $= 1$). When this value surpasses unity, air is said to be super-saturated due to the overabundance of water vapour. Therefore, it is possible to have super-saturated air either by increasing the vapour pressure or by decreasing the temperature (decreasing $e_s(T)$). Generally, it is easier to attain super-saturation by cooling rather than by increasing vapour pressure due the nature of the exponential dependence of $e_s(T)$ with regard to T (Clausius-Clayperion Equation [41]).

There are two processes that water molecules go through to achieve condensation, namely homogeneous nucleation and heterogeneous nucleation. Homogeneous nucleation can be described as a change of phase from pure water vapour to a droplet or ice particle phase without the intervention of any external substance. This process usually takes place abruptly following a string of fluctuations of temperature and density in the original phase, provided critical super-saturation of water vapour or a critical supercooling of water drops is achieved. This type of nucleation of water droplets in super-saturated vapour has never been observed in nature due to the extremely high values of super-saturation that are required to initiate growth for these tiny drops (less than $\sim 1\,\mu$m) [41]. But homogeneous ice nucleation in supercooled water droplets is known to be the governing mechanism in cirrus clouds. The critical temperature at which ice nucleation is initiated in these clouds is called the limit of homogeneous freezing of pure water droplets, the value of which is typically below $-35\,^{\circ}$C .

It has been observed that water can also nucleate on small water soluble particles called cloud condensation nuclei (CCN). Nucleation and growth through adsorption of water on such particles is called heterogeneous nucleation. In nature, two types of CCN are found. The first type being binary condensation nuclei such as $H_2O{-}HSO_4$, $H_2O{-}HNO_3$ and $H_2O{-}$NaCl that are generated from processes like incineration, lightning, and evaporation of sea water; the second type being dust particles (organic/biological or non-organic). Unlike homogeneous nucleation, heterogeneous nucleation does not require high

super-saturation values. In certain cases, at relative humidities slightly lower than 1.01 (101% R. H), it is possible to satisfy the growth activation condition for embryos that are as small as 1 µm in radius. In the case of dust particles and certain ionic binary CCN, the required activation humidity could be much lower than unity (100% R. H). This can be explained through Raoult's Law in thermodynamics, according to which the saturation vapour pressure of water containing a solute is reduced from the pure water value by a factor that depends on the molar concentration of the solute [41]. As long as the relative humidity of the surrounding environment is higher than the equilibrium relative humidity (E. R. H) [1] of the water droplet, there will be unbounded growth [42].

1.3 Summary of related contemporary research

Between (CCN) such as dust particles and ion clusters, we wish to concentrate on ion clusters, more specifically, ions that form binary H_2O-HNO_3 clusters after the laser induced ionization of the saturated air in the active filament volume. The most important properties and roles of solutes in condensation phenomena have been briefly discussed in the preceding sub-section using theories such as Raoult's Law, Kohler theory, among others. Under normal circumstances, the ions get adsorbed into pre-existing water clusters or micro droplets and contribute to the lowering of activation humidity threshold, thereby favouring unbounded growth. The equations in Table 1.1 were presented by the Teramobile group in [48] to map the chemical pathways leading to the generation of HNO_3.

The Table 1.1 presents the chemical equations and some of the possible pathways proposed by the Teramobile group [48] that can lead to the production of nitrates or nitric acid during the post-ionisation period in an air-vapour mixture. The components with "*" appended are in an excited state. "M" represents random molecules with which collisions could occur after ionisation. These equations were put forth based on experimental measurements of O_3,

1. The equilibrium relative humidity is defined as the relative humidity of the surrounding atmosphere when a substance (water droplet) neither gains or loses moisture.

Chemical Reaction Channels	
$N^+ + O_2 \rightarrow NO^+ + O^*$ (43%)	$e + N_2^+ \rightarrow N^* + N$
$N^+ + O_2 \rightarrow N + O_2^+$ (51%)	$N_2^* + O^* \rightarrow NO + N^*$
$N^+ + O_2 \rightarrow NO + O^+$ (6%)	$N^* + O_2 \rightarrow NO + O^*$
———————————	$e + O_2 \rightarrow O^* + O^*$
Oxidative Reactions	Generation of Hygroscopic HNO_3
$O^* + O_2 + M \rightarrow O_3 + M$	$NO_2 + NO_3 + M \rightarrow N_2O_5 + M$
$NO + O_3 \rightarrow NO_2 + O_2$	$N_2O_5 + H_2O \rightarrow 2HNO_3$
$NO_2 + O_3 \rightarrow NO_3 + O_2$	$3NO_2 + H_2O \rightarrow 2HNO_3 + NO$

Table 1.1: Chemical equations leading to generation of HNO_3 [48]

NO and NO_2 that were generated by a femtosecond filament inside an air filled plexiglas cell. Significant concentrations as high as 10^{16}, 3×10^{14} and 3×10^{15} cm^{-3} were measured using particle analyzers, resulting in concentrations of HNO_3 in the multi-ppm range. Computer modelling was done for this multi-ppm HNO_3 mediated laser-induced condensation [51]. It was found that as the concentration of HNO_3 increased, the required activation humidity value decreased. In the absence of HNO_3, it would take a relative humidity value that is slightly above the unity (100% R. H) to initiate growth. At 4 ppm, the model indicated that droplet growth can be initiated for values of R. H as low as 75%. It was also shown at higher concentrations of HNO_3 that the droplets reached larger diameters at a quicker pace. For example, the average time taken for a droplet of $\sim$0.05 µm diameter to reach $\sim$10 µm was close to 10 seconds.

Recent developments in SIOM have shown that the repetition rate of the laser filament has a very important role to play in laser-induced condensation [57–59]. 9 mJ/50 fs laser pulses working at a repetition rate of 1 kHz were focused into a commercial diffusion cloud chamber ($0.5 \times 0.5 \times 0.2$ m^3) filled with ambient air. The temperature gradient was found to vary from $-46\,^{\circ}$C at the bottom to ambient room temperature ($\sim 20\,^{\circ}$C) at the top of the chamber over a vertical distance of 20 cm. An f/70 cm concave mirror was used to focus

the beam inside the chamber and this gave rise to a $\sim$10 cm long filament [57]. A 10 Watt probe beam laser working at 532 nm wavelength was used to probe the laser interaction zone. The filament was shot at a height of $\sim$1 cm from the cold plate ($-29\,^{\circ}$C , 127% R. H). After a period of 30 minutes, formation of snow and ice piles in an area of 2.0 $\times$ 1.5 cm^2 below the filament were observed. The mass of this snow pile was measured to be $\sim$13.0 mg and the pH was found to be $\sim$2.0 using pH papers ($\sim$0.01 mol/L) [57]. The chemical mechanism for the presence of HNO_3 postulated by the Teramobile group was verified using pH paper and ion chromatography. A turbulence pattern characterized by intense updraft and convection of air, and by cyclic motion of tiny droplets, was observed in the filament volume with and without digital camera. The images taken during the experiment were used to measure velocities of the light diffusing particles. Droplets, at sizes as large as 30 µm, were found to travel at speeds as high as 60 cm/s. Laser-induced snow was observed using a 1 kHz laser train that was chopped, with a beam chopper, at rates of 150, 15, 5, and 1 Hz. At these chopping rates, hardly any snow was seen when compared to the complete 1 kHz train. More recently, simulations have been done in SIOM to understand the air-flow motion induced by femtosecond filaments inside a diffusion commercial cloud chamber [59]. The experimental parameters from [57–59] were used for this simulation, viz., 1 kHz, 9 mJ, 10 cm long filament. In this two dimensional simulation, after fixing the filament as a simple heat source, the flow fields in the whole chamber were calculated. Equations of coupled energy, mass and moment transports were used and numerically evaluated using the commercial software Fluent 6.3. The heating time and heat flux were set to 1 µs and 2 $\times$ 10^4 W/m^2 respectively. The thermal conversion efficiency of the filament was fixed at 5% [59] and chopping rates of 1, 5, 15, and 150 Hz were maintained just as in the case of the above mentioned experiment. The simulated results were in agreement with the experimental results barring the 1 kHz condition for which inconsistencies were found in the quantitative values. Nevertheless, the flow fields in the simulation were similar to the trace lines of the particles in the experimental pictures. Thus, both the simulation data and experiment results

point to the thermally sustained turbulence as a key mechanism in laser-induced condensation physics. Further exploration of this turbulence has been done and is presented later in this dissertation.

Chapter 2

Laser system

The experiments were done using an 800 nm laser beam that had a pulse width of $\sim$40 fs produced by a commercial laser system purchased from *Spectra-Physics*. The schematic flow chart of the laser system is presented in 2.1. This system is based on a typical *Chirped Pulse Amplification* (CPA) design with a seed emanating from a mode-locked titanium sapphire [1] laser oscillator [2]. The oscillator, as shown in 2.2, is composed of a Ti-sapphire crystal, two pairs of prisms to compensate dispersion, and an acousto-optic modulator (AOM) to initiate the Kerr lens mode locking. The titanium sapphire crystal is placed between two focusing mirrors F_1 and F_2 in the oscillator cavity and is pumped using a frequency doubled neodymium-doped yttrium orthovanadate [3] CW laser [4] of 532 nm wavelength. The pump beam is focused in from outside the laser cavity through the first focusing mirror F_1 into the Ti:Sapphire rod and is then sent out of the cavity through the second mirror F_2. At low intensities, for the cavity beam, these focusing mirrors are non-confocal in the CW regime but they become confocal in the pulsed regime due to the Kerr lens. In this pulsed regime, the losses are reduced over each round-trip and long-term stability is achieved. The AOM in the oscillator is used to initiate mode locking by destroying the initial stationary waves in the cavity. The AOM will then modulate losses in

1. Titanium Sapphire : Ti:Al_2O_3
2. Tsunami model, Spectra-Physics
3. Neodymium-doped Yttrium Orthovanadate : ND:YVO_4
4. Millennia Vs J Model, Spectra-Physics

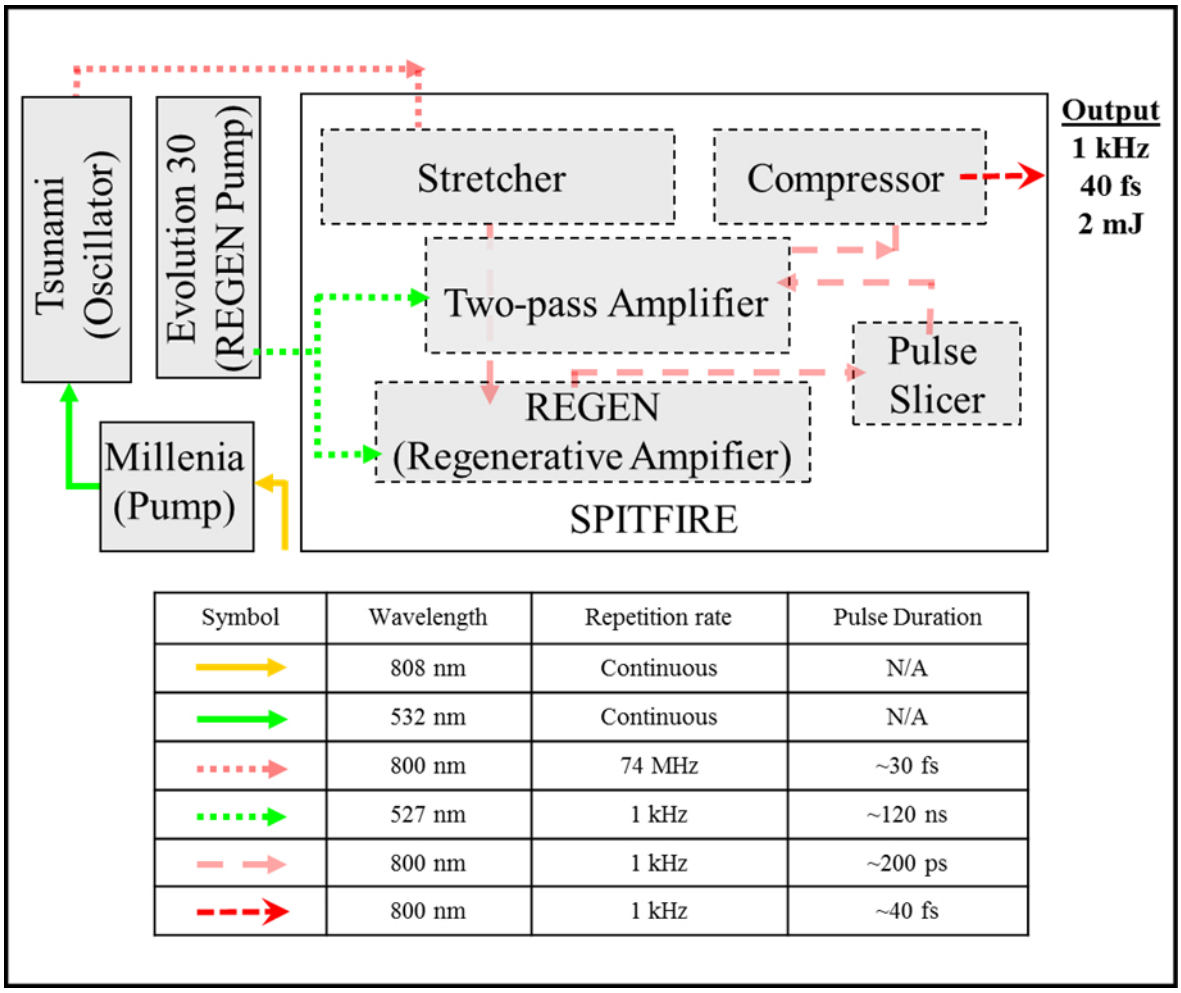

Symbol	Wavelength	Repetition rate	Pulse Duration
→	808 nm	Continuous	N/A
→	532 nm	Continuous	N/A
⇢	800 nm	74 MHz	~30 fs
⇢	527 nm	1 kHz	~120 ns
⇢	800 nm	1 kHz	~200 ps
⇢	800 nm	1 kHz	~40 fs

Figure 2.1: Schematic flow chart description of the laser system at the COPL lab in Laval University

the cavity in the temporal domain by letting through the phase locked components of the femtosecond pulse on each round-trip and diffract out the CW part. Once the mode locking is initiated, it can sustain itself through Kerr mechanism induced Self Phase Modulation (SPM) in the crystal and the AOM can be switched off. The oscillator produces linearly polarised pulses of ∼5 nJ energy and ∼33 fs duration at a repetition rate of 74 MHz, the pulse bandwidth is around ∼42 nm and is centered at ∼798 nm.

The pulses coming from the oscillator are then sent to the *Spitfire* system, as illustrated in Figure 2.3, that consists of a pulse stretcher, regenerative amplification stage, a 10 Hz pulse slicer, a two pass amplification stage and a pulse compressor. The pulse stretcher is based on

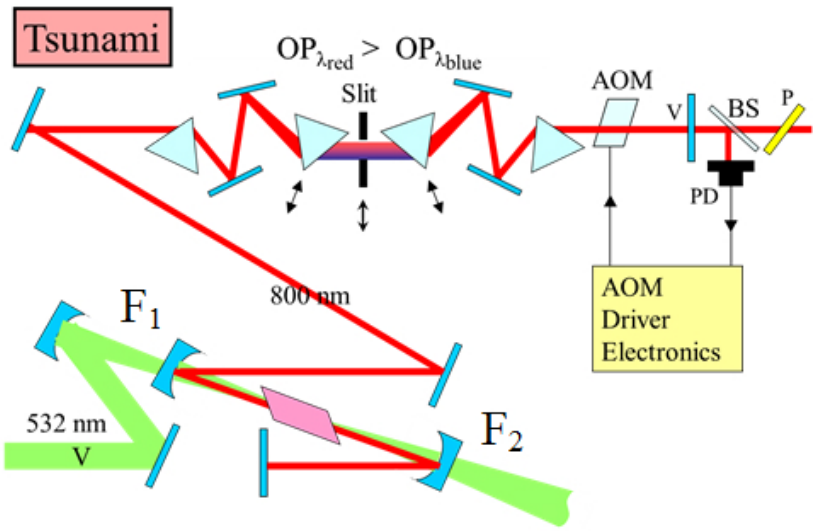

Figure 2.2: Optical Schematic of the commercial *Tsunami (Spectra-Physics)* oscillator. Courtesy: Dr. Francis Théberge.

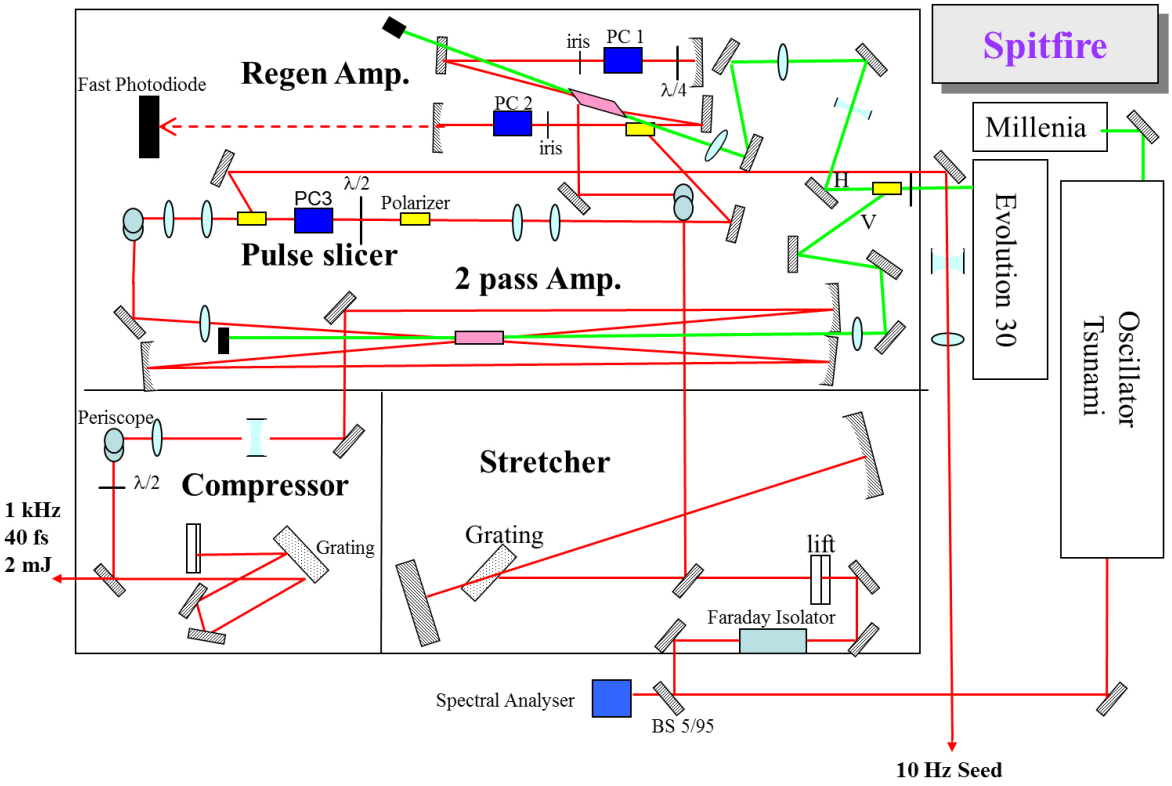

Figure 2.3: Optical diagram of the commercial laser chain *Spitfire (Spectra-Physics)*. Courtesy: Dr. Francis Théberge.

a design in which the pulse is stretched through multiple passes on a single grating and a concave mirror (optimized 4F system) from ∼33 fs to ∼200 ps. The pulse stretcher temporally delays the different spectral components with a quasi-linear phase relationship. In this case, the pulse is positively chirped, meaning that the lower frequency components can be found at the leading edge and as we move towards the trailing edge the frequency will increase. Stretching of the pulse reduces the laser peak power by a factor of $\sim 10^4$ and by doing so it is possible to extract a maximum of energy from the regenerative amplifier (REGEN) by preventing rapid gain saturation. From the ∼74 MHz pulse train, a pulse is trapped by the regenerative amplifier every millisecond using an electronically controlled Pockels cell. The REGEN is basically a Z-shaped laser cavity having a Ti-sapphire gain crystal pumped using nanosecond pulses also coming at a rate of 1 kHz from a Q-Switched and frequency doubled Nd:YLF laser (@527 nm). After multiples passes in the cavity, the pulse is extracted with a second Pockels cell when the peak power reaches a maximum value on the oscilloscope, viz., 1.5 mJ energy at REGEN output. After this stage, a pulse slicer working at 10 Hz sends out a pulse in every hundred to another system for further amplification. The ∼1 kHz pulse train is further amplified in a two pass system which uses a Ti-Sapphire crystal as gain medium. In the crystal, asymmetrical thermal lensing is induced by the high pump energy. This leads to deterioration of the beam quality. More precisely, the spatial profile of the beam tends to become slightly elliptical. The energy of the pulse is slightly lower than ∼3 mJ at the output of the two pass amplifier and in the following step the pulse undergoes compression in a pulse compressor. The compressor is based on a four grating design that has been simplified into a single grating system using symmetrical properties. The compressor sets back all the delayed frequency components of the stretched pulse back into phase (Fourier transform limited condition) and in doing so the shortest pulse (∼42 fs) with a maximum energy (∼2 mJ/pulse) is obtained from the system. The working model of the complete laser chain is presented in Figure 2.4.

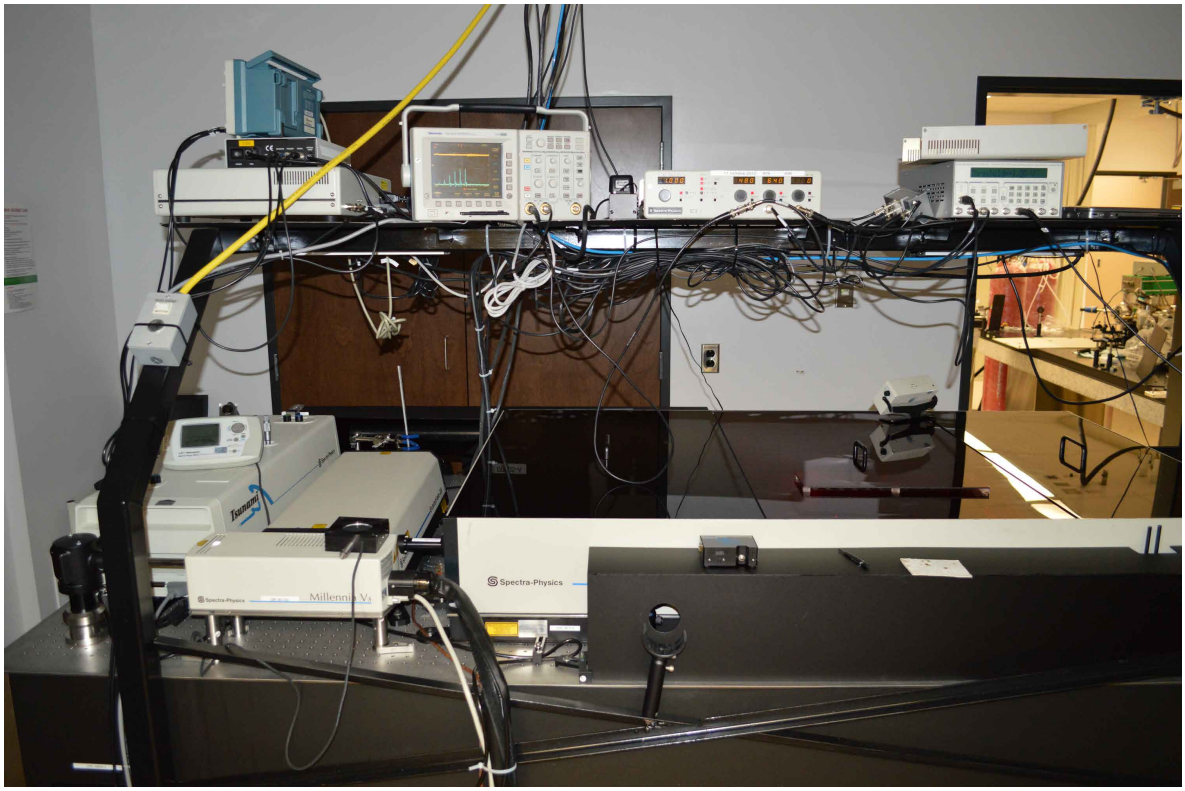

Figure 2.4: Image of the 1 kHz laser system at the COPL lab in Laval University

Chapter 3

Nitrate adsorption measurement

In this experiment, there were two main objectives. The first one was to understand the nature of the sub-saturated conditions and see if the filament gave rise to any visible effects. The second one was to verify if the chemical pathways (binary H_2O-HNO_3 cluster production) proposed by the Teramobile group were also valid in the inverted cloud chamber. To this end, an experimental setup was designed and the thermodynamic situation inside was assessed. As far as the first objective is concerned, pictures were taken inside the chamber with the filament using a digital camera. Tiny mist packets were observed upon exposure to the probe laser. Regarding the second objective, ion chromatography was performed on samples collected from a receptacle that was placed below the filament. Tiny droplets were seen falling on it with and without digital camera. Thus, the presence of NO_3^- ions in the samples would have confirmed the existence of the pathways proposed by Teramobile.

3.1 Experimental setup

The setup shown in Figure 3.1 was used for the nitrate adsorption measurement experiment. Pulses were focused into the chamber using a plano-convex lens of 50 cm focal length such that a filament of $\sim$2 cm length was created in the middle of the cloud chamber.

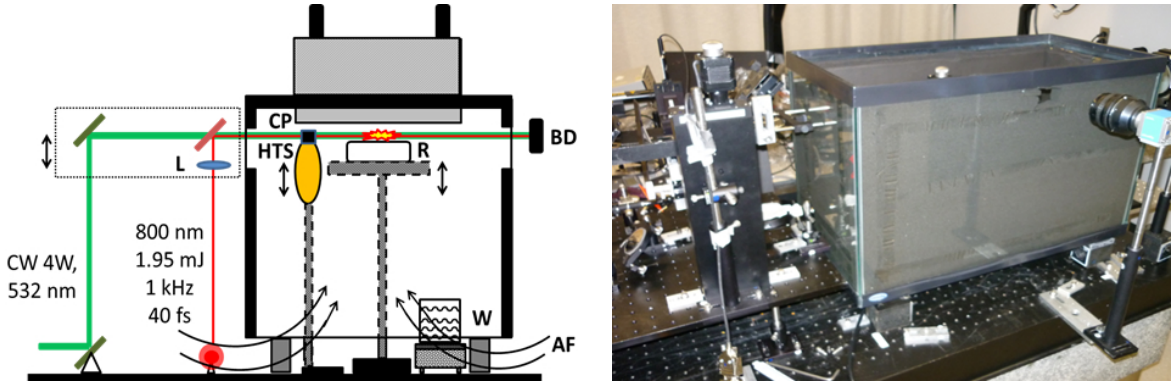

(a) **(b)**

Figure 3.1: (a) Schematic of experimental Setup for Nitrate Absorption Experiment (Open Chamber). Expanded form of acronyms: CP – Cold Plate, BD – Beam Dump, L – 50 cm convex meniscus lens, AF – Air Flow from outside, R – Receptacle, W – Water heated with hot plate to $\sim$35 °C , HTS – Relative humidity and temperature sensor and **(b)** Real picture of experimental setup (without cold plate on top)

A CW laser [1] beam at a wavelength of 532 nm, with a diameter of 8 mm and an output power of 4 W was also used to probe the interaction zone inside the chamber. The scattering of the probe beam in the interaction zone was recorded using a digital camera. A computer controlled translation stage was used to control the height of the beams. A plastic receptacle with a diameter of $\sim$10 cm and a height of $\sim$15 mm was placed $\sim$1 mm below the filament in the middle of the chamber to collect any condensation residue. The height of this receptacle was adjusted manually when the filament height was changed such that the distance between the filament zone and the receptacle was kept constant.

A glass container measuring 59 $\times$ 29 $\times$ 52 cm^3, insulated using black foam, served the purpose of a chamber in this experiment. The top of the chamber was covered with an aluminum plate of thickness of 3 mm, also insulated using black foam, in which a thermoelectric cold plate [2] of surface area 21.6 $\times$ 16.1 cm^2 was inserted. The advantage of this type of cold plate was that it could be placed in any direction or position and its

1. Coherent, Verdi Model
2. CP-200HT-TT model, TE technologies

performance would remain the same. The temperature of the cold plate was fully computer-controlled and the lowest temperature attainable on the cold plate during the experiments was $-18\,^{\circ}\mathrm{C}$. The chamber was designed to let in air from the outside through gaps at the bottom to reduce the overall water concentration inside and to obtain a sub-saturated atmosphere. Moreover, water was constantly heated and the temperature was kept at $\sim 35\,^{\circ}\mathrm{C}$ in a beaker placed at the bottom in order to maintain the relative humidity. A thermometer was used to measure the temperature and a hygrometer was used to scan the relative humidity and temperature profiles in the chamber.

3.2 Methods and analysis

The thermodynamic conditions in the cloud chamber were assessed. The profiles of temperature and humidity were measured inside the glass chamber, as shown in Figure 3.1, and the corresponding graphs are presented in Figure 3.2. Figure 3.2a shows the case where the air flow was sealed at the bottom of the chamber and Figure 3.2b presents the open condition with air flow. The position of the humidity sensor was changed every thirty minutes to a new position during the measurement of these profiles. The measurements were scheduled as follows.

Initially, the sensor was stabilized for 10 minutes. Then, after an elapsed time of 10 more minutes (20 minute mark), the first measurement of temperature and humidity in the chamber was taken. Then, these two parameters were measured once again after 10 more minutes (30 minute mark). The experimental errors of these measurements were determined by observing fluctuation over the last 20 minutes. The hygrometer, owing to an oversized sensor head, had to be placed at a minimal distance of 5 mm from the cold plate. One can notice in Figure 3.2 that the error bars are much longer when the measurement was taken at positions far from the cold plate. This indicates that the “natural” turbulence in the chamber causes the relative humidity to fluctuate as the distance from the cold plate increases. Thus, to avoid

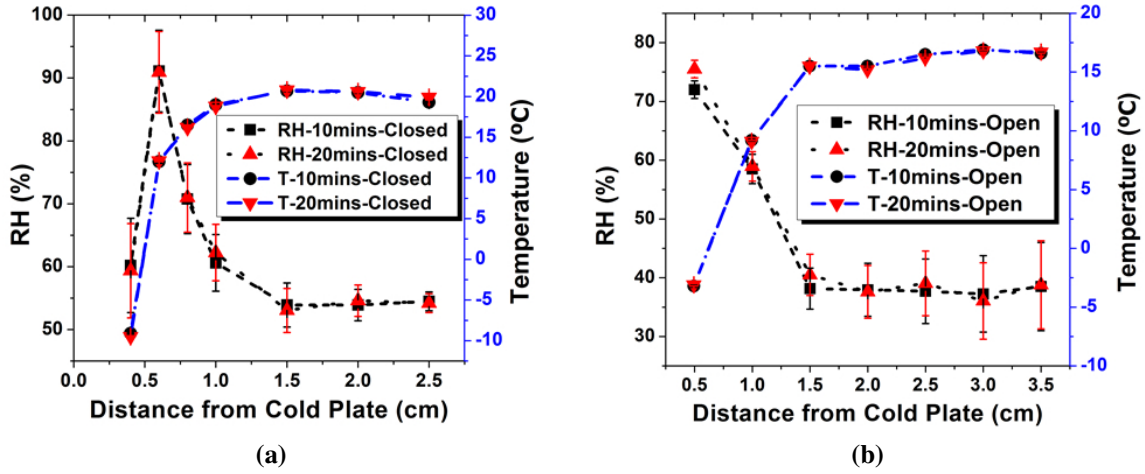

Figure 3.2: Relative Humidity (R. H) and Temperature (T) profiles versus distance from the cold plate for **(a)** the sealed chamber (no air flow) and **(b)** the open chamber (with air flow).

such unstable conditions, the laser irradiation was done at positions (distance between cold plate and filament) that are equal to or below 1.5 cm. The relative humidity in the lab was measured to be $\sim$24%. However, this value is not observed anywhere inside the chamber where the relative humidity is seen to drop rapidly and to stabilize at a mean value of 40% when the sensor was moved further away from the cold plate.

The receptacles used for the experiments were cleaned in advance using ultrapure water in order to cleanse away dust particles and charged molecules. Nitrate mass measurements were performed in two steps. In the first step, the condensate in the receptacle and the mixture of snow and ice on the cold plate were collected in the absence of a laser filament after a waiting period of 90 minutes. In the second step, the first step was carried out in the presence of a laser filament. The snow and ice on the cold plate were melted and collected separately after removing the cold plate. Subsequently, the four collected samples were subjected to ion chromatography tests. The irradiations were done at distances of 0.5 cm, 1.0 cm (0.9 cm for the closed chamber), and 1.5 cm from the cold plate for both closed and open conditions of the cloud chamber. The receptacle was positioned manually on every occasion.

A digital camera was used to record the Mie side scattering of the probe beam in the

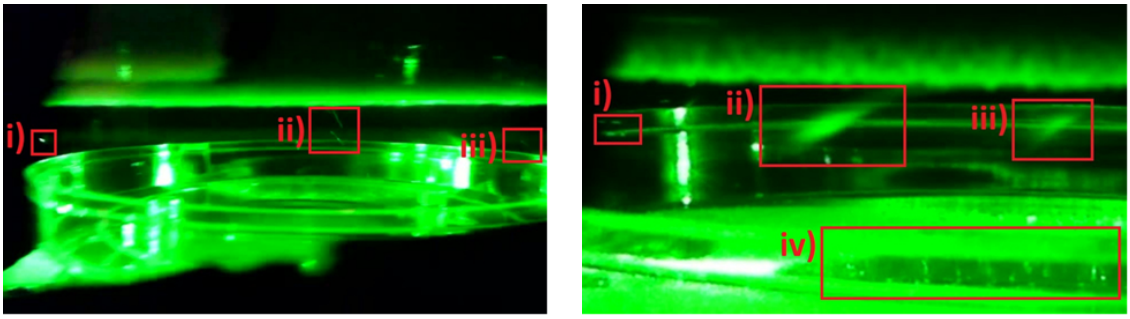

(a) **(b)**

Figure 3.3: **(a)** Side Mie scattering in absence of filament showing random droplets in i), ii), and iii) and **(b)** Side Mie scattering in presence of filament showing random droplets in i), ∼1 cm long mist packets in ii) - iii) and droplets in the receptacle in iv), filament of ∼2 cm approximately in between boxes ii) and iii) but invisible to the camera.

chamber during each experiment. Turbulence created by the filament similar to the one observed in the SIOM experiment could be seen [57]. Figure 3.3a shows the condition inside the closed chamber without irradiation and Figure 3.3b presents the case with irradiation (filament). The pictures were extracted from a video shot at 14 frames per second. On the one hand, Figure 3.3b presents traces made by droplets generated in the cool saturated zone travelling in random directions at random velocities. On the other, a filament gives rise to small mist packets that travel in the direction of the incoming laser. In the case of Figure 3.3b, the mist packets travel towards the left. Many of these droplets fell into the receptacle; however, others got dispersed all over the chamber. During the experiment, the scattering due to the natural and filament-induced turbulence in the chamber has been observed with and without a digital camera. The trail behind the mist packet is a result of a very low frame rate and prolonged exposure of the camera.

During and after irradiation, very small droplets that evaporate immediately after their apparition could be clearly identified on the receptacle. The temperature at the receptacle height was not low enough to conserve them. Some droplets could be seen at the bottom of the receptacle, as shown in Figure 3.3b. The droplets should have come from the super-saturated region near the cold plate after the filament induced HNO_3 molecules were generated and

dispersed throughout the inverted chamber [46, 57]. Despite the fact that very few measurable water droplets were left in the receptacle once it was taken out of the cloud chamber, it was assumed initially that if the filament induced water droplets had fallen into the receptacle and evaporated, the evaporation would have left behind some traces of HNO_3. According to recent work done by the Teramobile group [46–53] and the work in SIOM [57], HNO_3 is the seed of nucleation and condensation of the water droplets. To this end, the nearly empty receptacle was rinsed using ultrapure water (Nanowater) and the solution thus obtained was transferred to a cleaned plastic container and diluted to a volume of 6 ml. Then, three identical solutions, made from this solution, were subjected to ion chromatography tests to get absolute concentrations (mg/l) of NO_3^- present in each sample from which the absolute mass of HNO_3 was determined. Measurements were performed on these samples using an ion chromatograph [3] to determine the mass of NO_3^- present inside the receptacle and on the cold plate. The ion chromatograph was calibrated using aqueous potassium nitrate (KNO_3) standards. The results are shown in Figure 3.4a and Figure 3.4b. The error bars ($\pm 1\sigma$, where σ represents the standard deviation) were obtained using the uncertainty on the slope and intercept of the calibration curve calculated by linear regression. The reactions in the oxidative chemistry of nitrogen triggered by filamentation during the generation of HNO_3 have been previously proposed and confirmed by Kasparian et al. [46–53] and reconfirmed by Ju et al. [57–59]. In the next paragraph, we propose to undertake a comparison of the production of HNO_3 in the experiments done by Kasparian et al. and Jingjing Ju et al. [48, 57], and that of our experiments.

Using the value for the amount of molecules of NO_2 of 3×10^{13} molecules/pulse provided by Teramobile [48] and the values for the mass of the snow pile measured at $\sim$12 mg and nitrate concentration measured at HNO_3 concentration (0.032 mol/L) over a surface of 1.5 $\times$ 2.0 cm^2 given by SIOM [57], we estimated the number of molecules of HNO_3 created per

3. Dionex Model ICS 1000 equipped with a Model AS40 automated sampler, Model IonPacAS14A 4 $\times$ 250 mm Anion-Exchange column and Model DS6 Heated conductivity cell detector

second in the active filament volume. The values are presented in Table 3.1.

Using the experimental results of the Teramobile group, an upper limit for the number of molecules of HNO_3 per laser pulse in the active filament volume was obtained based on the assumption that all the NO_2 got converted into HNO_3. Therefore, 3×10^{13} molecules of NO_2 per pulse would result in 6×10^{13} molecules of HNO_3 per pulse and in 6×10^{14} molecules of HNO_3 per second, taking into account the 10 Hz repetition rate of their laser beam.

In our case, as was the case at SIOM, it was possible only to get a lower limit for the production of HNO_3 molecules, as a cloud chamber was used in both cases. In a closed cloud chamber, since an unknown amount of this HNO_3 attached itself to various surfaces inside the chamber, not all the HNO_3 could be measured and as for the open cloud chamber the HNO_3 could even get ejected out of the chamber.

Using the values provided by SIOM for the mass density of the snow pile collected below the filament after laser irradiation (13 mg over a surface of 1.5×2.0 cm^2) and the concentration of HNO_3 in the snow pile (0.032 mol/L), we estimated the lower limit for the production of HNO_3, i.e. 1.4×10^{14} molecules of HNO_3 per second. The pH values of 2 and 3 for the snow on the cold plate in the area surrounding the filament were also given. Going by these pH values, we are of the opinion that the amount of HNO_3 molecules accumulated on the surface of the cold plate in the area surrounding the snow pile is quite significant. Since the amount of HNO_3 molecules in the area surrounding the snow pile is unknown, it is assumed that the total amount of HNO_3 molecules produced by the laser filament could be much higher than our estimations of the lower limit value shown in Table 3.1.

In our case, out of the data presented in Figure 3.4a, only the HNO_3 masses of $\sim$0.014 mg and $\sim$0.004 mg of the cold plate and the receptacle respectively, were taken into consideration for the estimation of the production rate. The estimated value of 3.2×10^{16} molecules of HNO_3 per second for the production rate is presented in Table 3.1. The production rate of

Research Group	Production of HNO_3 in filament volume (molecules/second)	Laser conditions
Teramobile [13]	$\sim 6 \times 10^{14}$ Direct measurement using analyzer	10 Hz, 12 mJ/pulse, 80 fs
SIOM [19]	$>> 1.4 \times 10^{14}$ From snow pile on cold plate	1 kHz, 9 mJ/pulse, 50 fs
COPL	$> 3.2 \times 10^{16}$ From cold plate and receptacle	1 kHz, 1.95 mJ/pulse, 40 fs

Table 3.1: Experimental values of the number of HNO_3 molecules per second estimated from the work of each research group

HNO_3 was higher in the two cases using 1 kHz beams.

The data, as shown in Figure 3.4, confirms the same observations made by researchers at SIOM [57], i.e. filamentation did induce the formation of HNO_3, as represented by the red and pink lines of Figure 3.4a and Figure 3.4b, and the amount of HNO_3 found inside the receptacle and on the cold plate was nil in the absence of the filament, as shown in bottom lines of Figure 3.4a and Figure 3.4b. Our explanation of the phenomenon of formation of HNO_3 can be formulated thus: as the filament is moved away from the cold plate, the amount of NO_3^- found on the cold plate decreases and remains almost constant inside the receptacle for both cases of closed and open chambers. When the filament is near the cold plate, the humidity is higher and a greater quantity of HNO_3 is produced. Moreover, its proximity to the cold plate implies that a significant amount of HNO_3 will be pushed up into the super-saturated zone near the cold plate and will thereafter stick to the cold plate. Owing to the negligible quantity of HNO_3 in the receptacle, the relationship between the production of HNO_3 and the height of filament cannot be satisfactorily explained. Despite such shortcomings, it can be said that HNO_3 has been created during the filamentation process. Upon close observation of mist packets and water droplets collected in the receptacle, shown in Figure 3.3b, it became clear that condensation occurred after filamentation in the sub-saturated zone. A fresh experiment was carried out to confirm the

existence of condensation by attaching a cold finger below the receptacle.

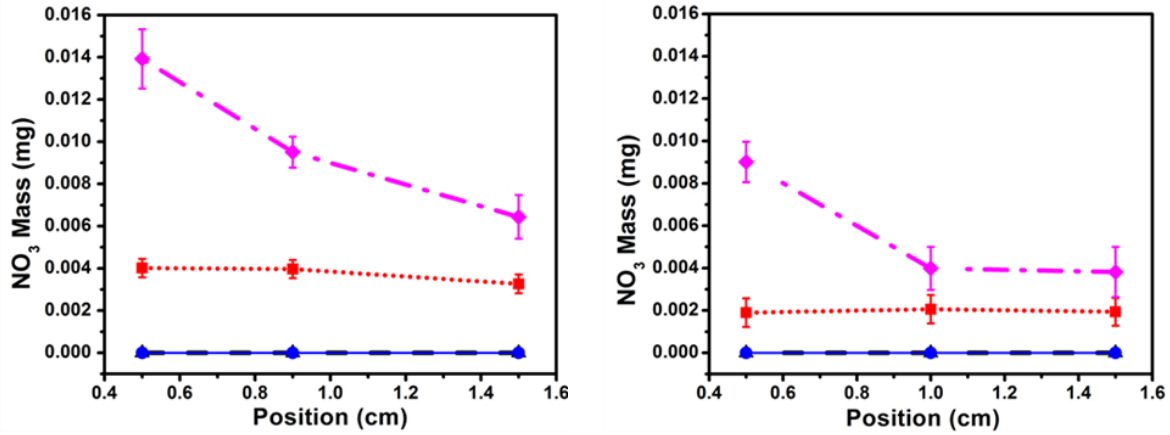

Figure 3.4: Nitrate mass versus distance from plate for **(a)** closed chamber (no air flow) and **(b)** open chamber (with air flow), Top most curve – mass on plate with filament, dotted curve – mass in receptacle with filament, bottom most curves – mass on plate and receptacle without filament

Chapter 4

Droplet growth measurement

In the previous section, it was demonstrated using the data obtained through ion chromatography that HNO_3 was invariably produced in the filament volume after the ionization process. Moreover, the 1 kHz laser beam produced significantly more of this cloud condensation nuclei, viz., HNO_3, compared to a 10 Hz laser beam , indicating that a high repetition rate is an important element in the production of HNO_3. However, in the context of that experiment, it was not possible to measure the growth in water mass induced by the laser filament. Two important obstacles had to be overcome in order to measure the growth in water droplets, namely the evaporation of water droplets caused by the warm temperature on the surface of the receptacle and the amplification of evaporation of water droplets caused by the natural air turbulence inside the glass chamber. The large volume of the chamber gave rise to more natural turbulence and was difficult to control. To this end, a more compact cloud chamber was designed in an attempt to minimize the evaporation. To ensure the conservation of the precipitate falling on the receptacle, a new cooling mechanism was used.

4.1 Experimental setup

The setup, as shown in Figure 4.1, was used in this experiment. All the components were used as in the previous experiment barring the cloud chamber. Since the glass chamber had

certain limitations owing to its larger dimensions, a compact plexiglas container of $26 \times 18 \times 30$ cm^3 was used to do this experiment. A detailed design of this container, shown in Figure A.1 of Appendix A, was done using SolidWorks software. The plexiglas chamber, unlike the glass chamber, allowed for the drilling of a set of holes that served the dual purpose of acting as aeration vents as well as laser windows. The aeration vents reduced the overall water content in the chamber and the relative humidity along the laser axis. Further modifications were made to the setup. A "U" shaped copper plate, that served the purpose of a cold finger, was attached to the cold plate on which the receptacle was placed. The cold finger helped to preserve the droplets falling inside the receptacle by maintaining the surface temperature at slightly below $0\,^{\circ}$C . The distance between the cold plate and laser filament was modified by stacking plexiglas spacers of 5 mm thickness between the roof of the chamber and the frame of the cold plate.

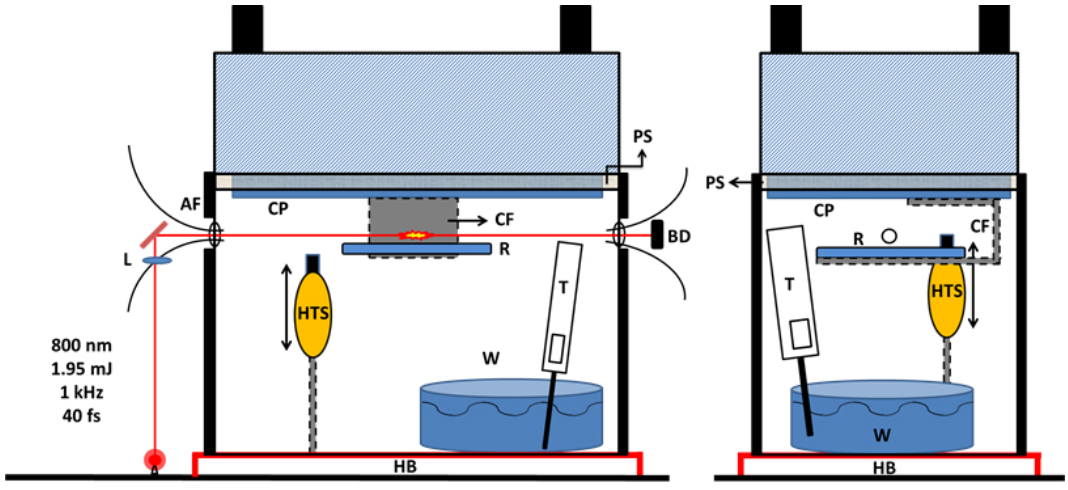

Figure 4.1: Front and side view of the experimental setup for the droplet growth experiment (Open Chamber). Expanded form of acronyms: CP – Cold Plate, BD – Beam Dump, L – 50 cm convex meniscus lens, AF – Air Flow from outside, R – Receptacle, W – Heated Water Bath at $\sim 35\,^{\circ}$C , HB – Hot Base, HTS – Relative humidity and Temperature sensor, T – Thermometer for Water Bath, CF – Cold Finger, PS – plexiglas spacer

4.2 Methods and analysis

The temperature of the cold finger was around $-5\,^{\circ}\mathrm{C}$. The distance between the filament and the cold plate was maintained at $\sim$1 cm during the laser irradiation. The height of $\sim$1 cm was maintained, since the relative humidity ($\sim$60% R. H) was sufficiently low for it to be considered sub-saturated. The natural turbulence at this height was found to induce very little fluctuations in relative humidity. Water was first collected without the laser filament over a period of 180 minutes. Subsequently, this process was repeated for the same duration with filament for a different receptacle. The data pertaining to this experiment is presented in Table 4.1. The mass of both the receptacles was measured immediately at the end. The values for the growth in water droplets were obtained by subtracting the mass of receptacle without filament from that with filament. The temperature of the water bath was maintained at $\sim 35\,^{\circ}\mathrm{C}$ as in the Nitrate Adsorption Measurement. As can be seen in Table 4.1, the amount of water found inside the receptacle was higher when the laser filament was present. The difference between the masses was found to be $\sim$0.95 g. The mass of NO_3^- was measured using ion chromatography at 0.0137 mg. This value is much higher than the one found in the first experiment due to the cooling induced by the copper cold finger. NO_3^- was not found in the receptacle when the filament was absent. Evaporation that occurred during droplet accumulation was minimized thanks to the cold finger fixed under the receptacle, but evaporation during transportation was unavoidable. In all these experiments, the receptacles were carried from the laser laboratory to a chemistry laboratory for sample collection and mass measurements. Since the transportation time was only a few minutes and the receptacles were tightly sealed using aluminum foil during transportation to minimize any possible leak, it was thought that that very little water in the receptacle was lost due to evaporation.

The following model was initially proposed to explain the growth in water condensation that had been observed inside the receptacle. As the femtosecond laser pulses were fired into the chamber, a filament was created in the middle of the chamber. To produce binary

Water bath Temperature	Mass of liquid without Filament	Mass of liquid with Filament	Mass difference	Nitrate Mass inside receptacle with filament
(°C)	(g)	(g)	(g)	(mg)
35	0.8536	1.7539	0.9003	0.0137

Table 4.1: Measurements of condensate mass found inside the receptacle with and without filament.

clusters of HNO_3-H_2O, the individual molecular components of air such as O_2, N_2, CO_2, and H_2O were subjected to the oxidative chemistry process proposed by the Teramobile group [48] after various ionization and dissociation processes. These clusters then grew into cloud condensation nuclei (CCN) when kept close to the filament volume.

As observed by the SIOM group [57–59], the CCN were subsequently propelled throughout the chamber as a result of the heavy turbulence caused by the high repetition rate of the laser filament. Large quantities of these nuclei were sent upwards due to the convection induced by the high local temperature around the filament. The CCN were pushed towards the saturated zone near the cold plate and grew into larger droplets owing to the high water vapour concentration. A significant portion of these droplets became condensed on the cold plate and the remaining droplets fell down, some inside the receptacle causing the water mass inside to grow, as seen in Table 4.1, and some others elsewhere in the chamber.

Thus, the measurements done in this experiment clearly show the existence of amplification in condensation caused by the laser filament. This confirms our initial hypothesis predicting that the filament must have had some kind of an amplifying effect on the total water content inside the receptacle. However, two questions come to mind: what exactly is the nature of the turbulence inside the cloud chamber? How does turbulence influence the growth in condensation? In the next section, we have attempted to answer these questions with the help of a traditional cloud chamber.

Chapter 5

Turbulence analysis

In the last two sections, the following two elements have been demonstrated for the sub-saturated condition. It is possible to produce the binary H_2O-HNO_3 condensation nuclei required to reduce the activation humidity of the water droplets and it is equally possible to have enhancement in water condensation/precipitation despite the sub-saturated environment. Now the laser induced turbulence remains to be understood. Previously, the turbulence had been observed only for focusing elements (lens/mirror) of long focal lengths placed at the entrance of the chamber. This type of turbulence was observed both in experiment and in simulation by SIOM [57–59]. In this section, a systematic study of turbulence, done for lenses of different focal lengths, is presented to better understand the effect of focal length on turbulence. It was assumed that changes in the turbulence have certain consequences on the condensation/precipitation processes occurring inside the chamber. The results are presented along with theoretical support, obtained through simulations done at SIOM using similar experimental parameters. This chapter is based on the following article entitled "Laser-filament-induced snow formation in a subsaturated zone in a cloud chamber: Experimental and theoretical study", by Jingjing Ju, Haiyi Sun, Aravindan Sridharan, Tie-Jun Wang, Cheng Wang, Jiangsheng Liu, Ruxin Li, Zhizhan Xu, and See Leang Chin. This manuscript had been published in *Physics Review E* as this dissertation was being written.

5.1 Experimental setup

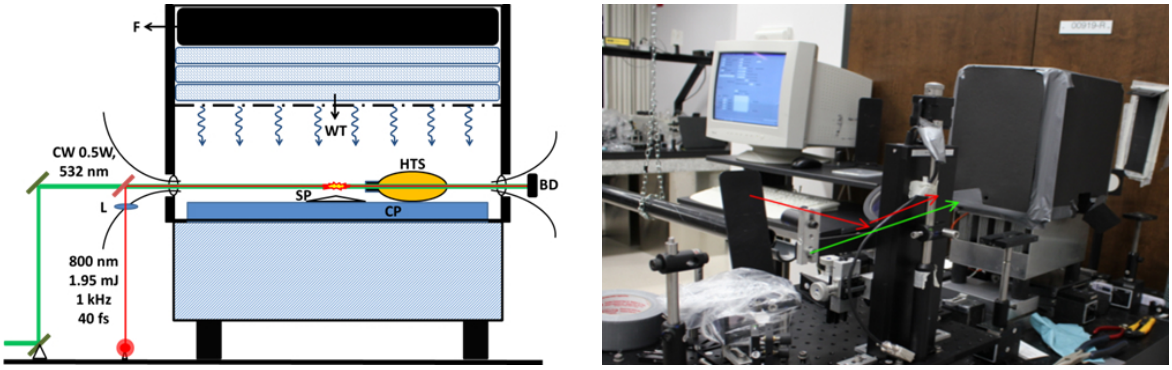

(a) **(b)**

Figure 5.1: **(a)** Front view of the experimental setup for turbulence analysis (Open Chamber). Expanded form of acronyms : CP – Cold Plate, BD – Beam Dump, L – 20/30/50/80 cm plano-convex meniscus lenses, HTS – Relative humidity and Temperature sensor, WT – Wet/Damp towels that act as vapour source, SP – Snow Pile, F – Foam for insulation and **(b)** Real picture of the experimental setup

The setup shown in Figure 5.1 was used to study the influence of turbulence on laser-induced condensation. The same plexiglas chamber of reduced dimensions (25 $\times$ 18 $\times$ 15 cm^3) as shown in Figure 4.1 was used for this experiment. The top of the plexiglas chamber was used as a wet towel compartment that was isolated from the rest by a metal plate that was uniformly perforated on the surface. In this experiment, water vapour was not produced through traditional methods. Instead, damp wet towels, placed on top of the metal plate, released moisture in the compartment below. These towels were washed using tap water and then squeezed until there was no more dripping. Enough moisture was retained in the towels in order to generate vapour in the chamber. Thick black foam that was used to insulate the glass chamber, as shown in Figure 3.1, was also used to cover the wet towels to prevent vapour leaking from the top. The laser was once again positioned, as in the previous experiments, at a distance of $\sim$1 cm from the cold plate. The temperature was observed to be 5.5 °C and the R. H was slightly higher than 75% on the laser axis. The co-propagating CW green laser, expanded to a size of 2.0 cm, was once again used to probe the area around the filament.

A digital camera was used to capture the images from the side of the chamber. A Pixel-Fly CCD camera was also used to capture the images of the filaments for each of the four lenses.

5.2 Methods and analysis

5.2.1 Effect of the focal length of the lens placed at entrance of the chamber

To understand the effect of laser-induced turbulence on condensation in sub-saturated conditions, a systematic experiment using four lenses was done initially. In the current experiment, the irradiation period for the laser was set to 60 minutes and four lenses with focal lengths of 20, 30, 50 and 80 cm were used to focus the beam in the chamber, as shown in Figure 5.1. The traditional temperature gradient was used here to observe the effect of the plano-convex lens on the formation of precipitation on the cold plate, if any. In the traditional cloud chamber used for the experiment, there is a pressure difference between the input and output laser windows, inducing a strong natural air current that is much weaker compared to the one existing in the inverted chamber. Hence, the traditional cloud chamber is better suited to observe filament induced turbulence. The CCD images of the filaments created by the four different lenses are presented in Figure 5.2. From Figure 5.2, it can be said that longer focal lengths give rise to longer filaments, but the intensity of the scattered light reduces with increasing focal lengths. More specifically, in the case of the f/80 cm lens, the white core of the filament is practically not observed. From the images shot using the four lenses, the laser-induced turbulence is expected to be different in each of these four cases.

Images of the filament area illuminated by a CW probe laser, as shown in Figure 5.3, were captured using a digital camera. The images of f/20 and f/30 cm lenses presented visible vortices beneath the filament, while no such pattern was seen for the f/50 and f/80 cm lenses. Moreover, the images of the snow piles for the f/20 and f/30 cm lenses, presented in

Figure 5.2: CCD Images of the laser filament in the setup shown in Figure 5.1 for f/20, f/30, f/50 and f/80 cm lenses at the chamber entrance.

Figure 5.4, were taken with the same camera. Using Figure 5.3, it is possible to calculate the maximum velocity of the particles in the area surrounding the filament. This was done by first finding the actual length of the trails left behind by the micro-droplets. The actual length of the trail is obtained by counting the number of pixels the trail occupies in the image multiplied by a calibration factor. The calibration factor can be obtained by placing a ruler in the image and by counting the number of pixels it occupies. If, for example, there are 40 pixels in 1 cm, then the calibration factor would be 1 cm/40 pixels $= 0.025$ cm/pixel. Based on the above calculations, the actual length was divided by the known exposure time of the camera to obtain the velocity of the particle. The maximum velocity of a particle recorded for each lens is shown in Figure 5.5a. When the f/20 cm lens was used, the highest speed of 16.5 cm/s was observed for the particles illuminated by the green laser. For the four lenses presented in Figure 5.3, the f/20 cm lens produced the cleanest and fastest turbulence pattern with two cylindrical vortices that formed right below the filament. For the f/50 and f/80 cm lenses, no vortex was present under the filament; however, a thick mist could always be seen slithering across the chamber right below the filament.

After the laser irradiation, the snow under the laser filament was checked for acidity using pH paper. The pH paper results indicated acid content for all four lenses and values of pH

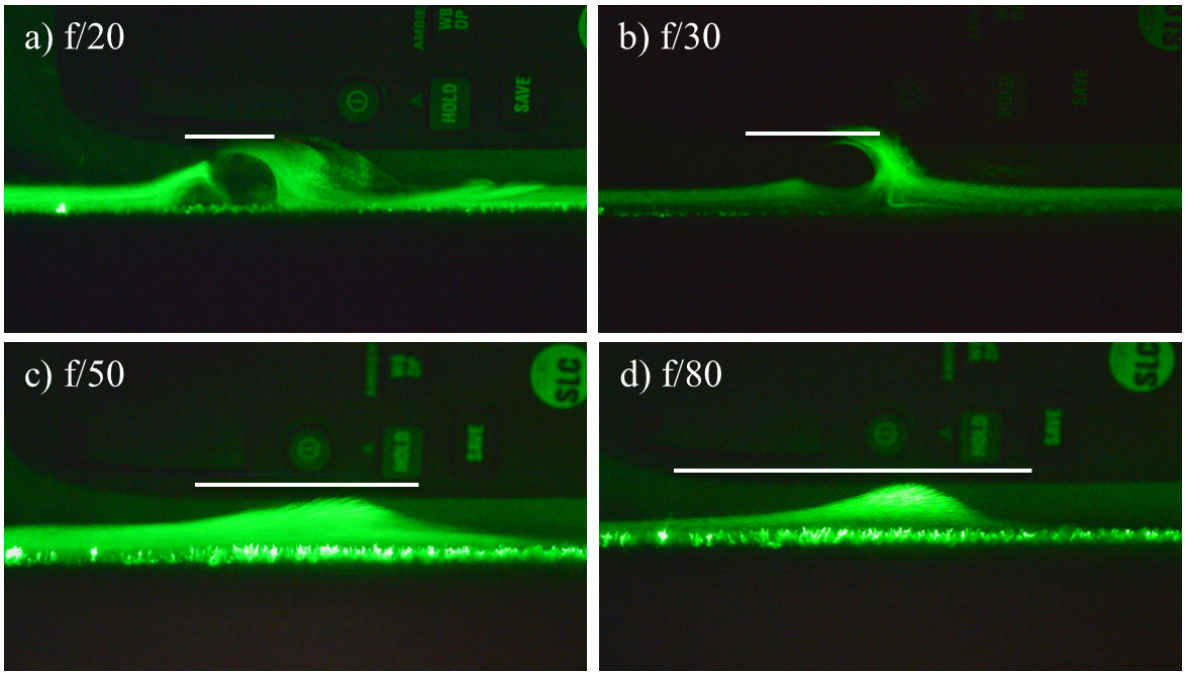

Figure 5.3: Digital camera images of the turbulence below the filament (white lines representing filaments have approximate lengths and positions)

ranged between 1.0 to 4.0, depending on the lens and place where it was measured. Results from ion chromatography tests that were done subsequently on the snow samples showed significant quantities of HNO_3 ($\sim$40 µg/L).

The mass of the snow below the filament was also measured and these values are plotted as a function of the focal length of the lens placed at the entrance in Figure 5.5b. Only the f/20 and f/30 cm lenses gave rise to clear distinguishable snow piles that could be measured using a mass balance. For the f/50 and f/80 cm lenses, the pile was practically absent and the mass values, as presented in Figure 5.5b, for these two cases are not accurate. It is to be noted that the largest pile was found for the f/20 cm lens and it had a peculiar elliptical shape. Moreover, the major axis of this ellipse was almost perpendicular to the laser propagation axis. From these results, the hypothesis that the focal length of the lens plays a significant role in the laser induced condensation process was verified. It can be said that the shortest focal length of f/20 cm produced the most interesting results from the following observations:

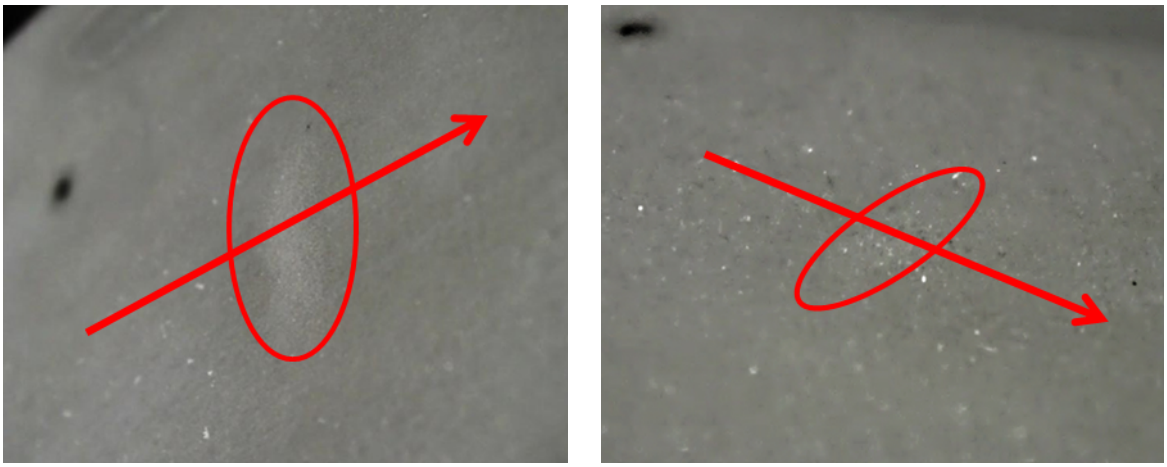

(a) **(b)**

Figure 5.4: Image of the snow pile below the filament for **(a)** f/20 lens and **(b)** f/30 lens (The red arrow shows the direction of the laser)

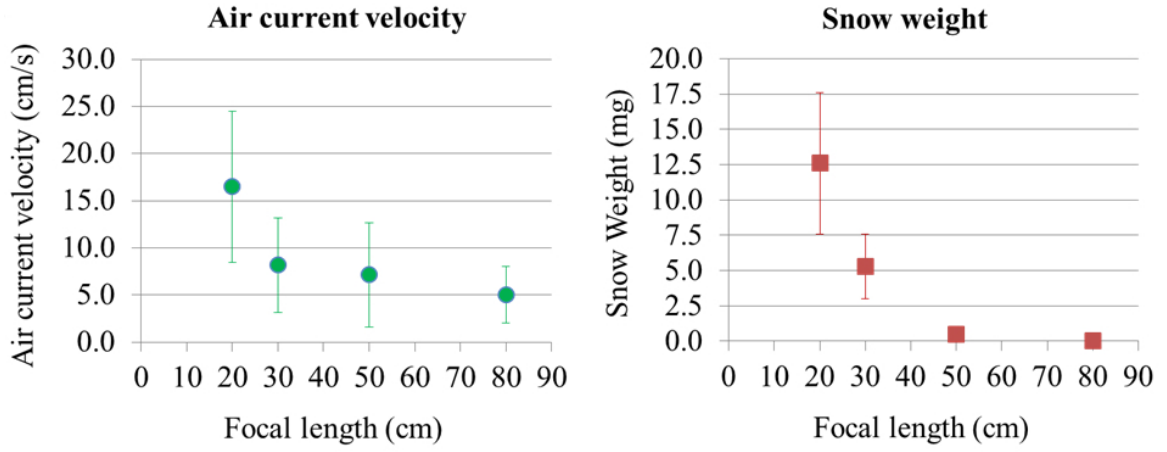

(a) **(b)**

Figure 5.5: **(a)** Mass of snow weight (mg) and **(b)** air current velocity (cm/s), versus focal length of input lens (cm)

the turbulence pattern for this lens contained two clearly distinguishable vortices that spun with a very high angular velocity. The largest snow pile in the form of an ellipse was observed in the above mentioned case. From these observations, it can be said that stronger turbulence could be an important factor in the laser induced condensation/precipitation process in sub-saturated conditions. The f/20 cm lens was further investigated in order to better understand the physical mechanisms behind this strong laser induced turbulence.

5.2.2 Simulation of laser induced-turbulence using the COPL cloud chamber parameters

In order to understand the nature of the vortices observed during the experiment, simulations on laser induced turbulence, using experimental parameters from COPL, viz. filament length of 1.1 cm, filament diameter of 120 µm, were run by our collaborator Haiyi Sun at SIOM. In addition, the laser filament was merely considered as a source of heat and that only 5% of the laser energy would be converted into thermal energy [59]. The simulation was done for two cross-sections passing through the centre of the filament. Each of these cross-sections was parallel to one of the two lateral surfaces of the chamber and perpendicular to the cold plate. The results from these simulations are shown in Figure 5.6 and Figure 5.7.

By looking at Figure 5.6 and Figure 5.7, two sets of loops in the turbulence pattern can be observed. They are formed when the hot filament creates a low pressure zone by rapid heating and, in consequence, by quick expansion of the surrounding air. This low pressure zone pulls in air from the lateral sides of the chamber, which gets split into two parts. This explains the formation of the upper and lower pairs of loops, as shown in Figure 5.6 and Figure 5.7. The distance between the bottom pair of loops, as shown in Figure 5.6, is $\sim$1.10 cm. The two loops formed during simulations closely resemble the loops, called vortices, formed during experiments, as shown in Figure 5.3 for a focal length of 20 cm. Based on the simulations, it could be said that the moisture released from the top of the chamber would

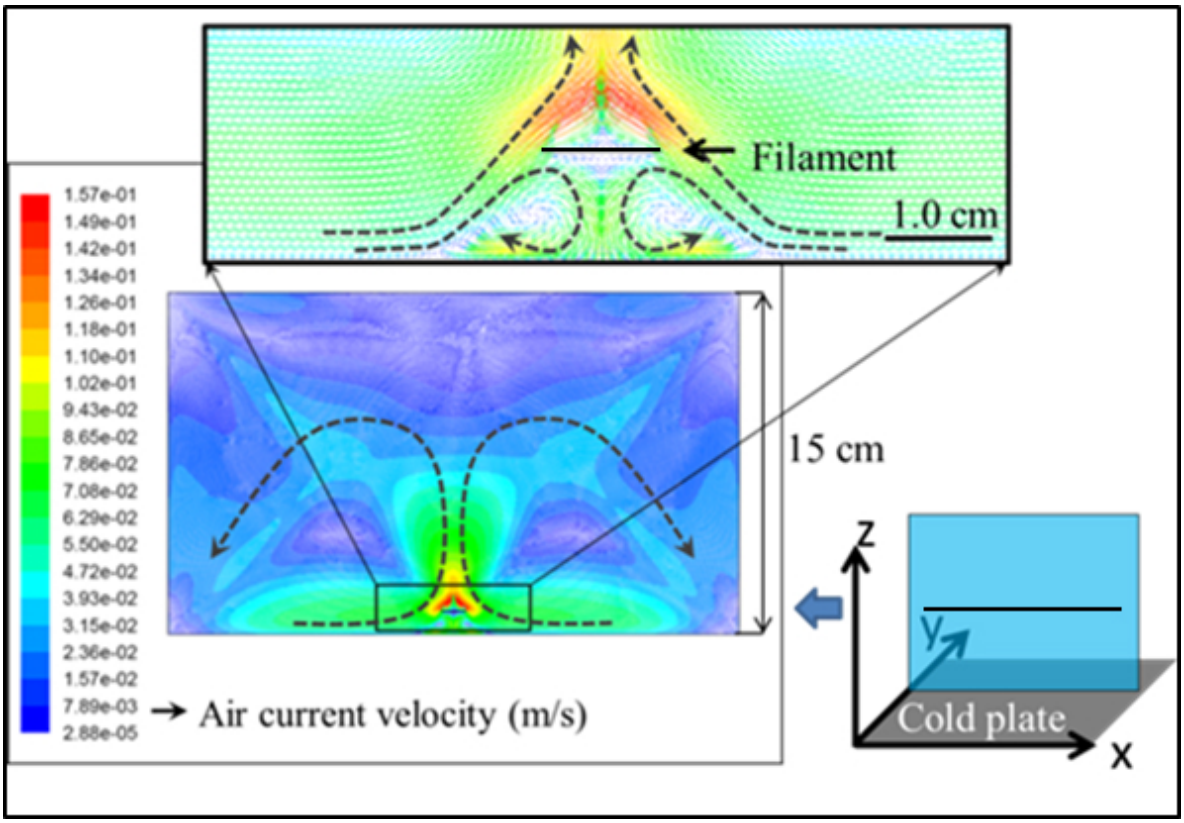

Figure 5.6: Two dimensional simulation done in the x-z cross-section plane containing the filament. The calculated air current velocity (m/s) generated by laser induced turbulence is given for each position inside the cross-section.

get pulled in by the bigger loops generated by the heat produced by the laser filament, and that the moisture will then be carried towards the filament by the downdraft where a part of it would get coupled into the smaller loops. Figure 5.8a depicts a typical scene of the turbulence observed experimentally using the f/20 cm lens under the conditions of $\sim$73% R. H and $\sim$4.35 °C . In this figure, there are two quasi-symmetrical vortices in the turbulence pattern and the centers of these two vortices are dark, unlike the peripheral areas. The absence of scattering at the center of the vortex is due to a lack of large-sized particles. Therefore, it can be inferred that the particles at the center are smaller than the probe wavelength ($<$ $\sim$0.5 µm) [60] by looking at the dark area around the epicenter. According to R. A. Shaw [60], water droplets, after having reached a critical value in size, tend to get spun out of the

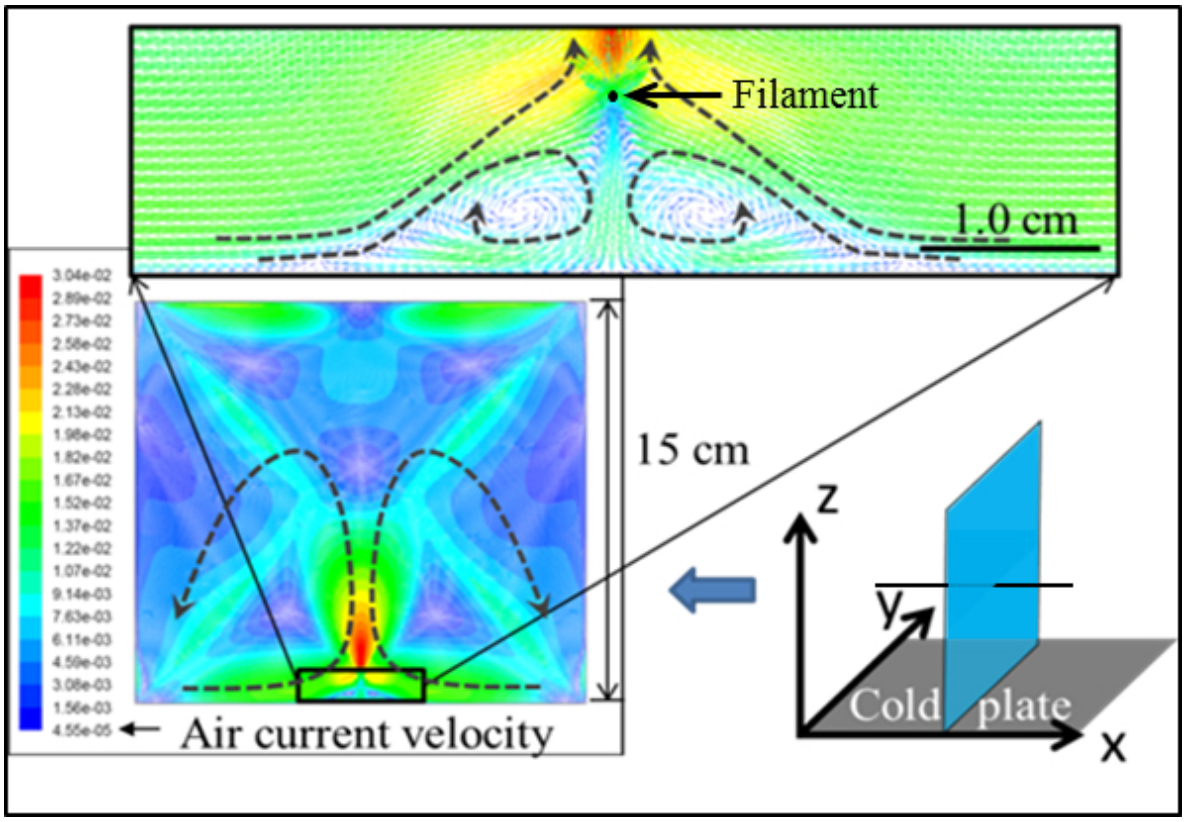

Figure 5.7: Two dimensional simulation done in the y-z cross-section cutting through the center of filament. The calculated air current velocity (m/s) generated by laser induced turbulence is given for each position inside the cross-section.

vortex. Consequently, there are very few water droplets large enough to scatter the probe beam. Moreover, larger droplets deplete the water vapor content at a higher rate than smaller droplets [60]. Thus, a vortex that is continually fed with moisture would tend to get saturated or even super-saturated near its epicenter. The scenario is represented in Figure 5.8b, in which, the horizontal dotted arrows represent the incoming moist air that is then shown to enter the vortices represented by the two green cylinders. The circular dotted lines have been used in the cylinders to represent the rotating direction of each vortex. The typical saturation profile has been plotted right below the vortices to illustrate that the epicenter of the vortices, unlike the edges, are saturated or super-saturated [60]. This saturated condition combined with the incoming CCN (dust and laser generated molecules like HNO_3, N_2^+, O_2^+) ensure

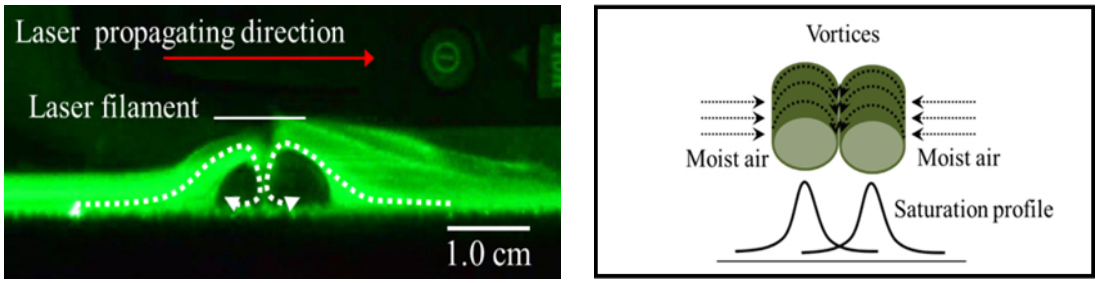

(a) **(b)**

Figure 5.8: **(a)** Scattering scene recorded from the side using a CW laser beam (532 nm, 0.5 W, 2.0 cm in diameter) revealing the two vortices below the filament. **(b)** A schematic diagram of the two vortices depicting the spinning direction of the moist air current (top, dotted lines and curves) and the schematic radial distribution of saturation ratio inside the vortices according to [60] (bottom, solid curves).

that the tiny droplets near the epicenter get immediately activated and start experiencing unbounded growth. As mentioned previously, these droplets get spun out of the vortices after reaching a critical size.

5.2.3 Three dimensional characterization of the turbulence

By looking at Figure 5.6 and Figure 5.7, a three dimensional view of laser induced turbulence can be visualised. If one takes the loops in the cross section and imagines a complete revolution of this cross section around a vertical axis that is placed at the filament center and is parallel to the 'z' axis, it would have a donut-like shape. Figure 5.6 and Figure 5.7 show that the distance between the epicenters is longer in the direction perpendicular to the filament. This would mean that the donut must be elongated in the direction that is perpendicular to the laser. In such a case, there would be an elliptical donut instead of a circular one. This elliptical donut with a major axis perpendicular to the laser filament is illustrated in Figure 5.9a. The top view of this donut is shown on the left hand side of Figure 5.9b and pictures of the turbulence taken for different illumination angles of the probe laser are shown on the right hand side. As the angle between the probe laser and the filament increases, the illuminated cross-section of the elliptical donut widens; the difference in the

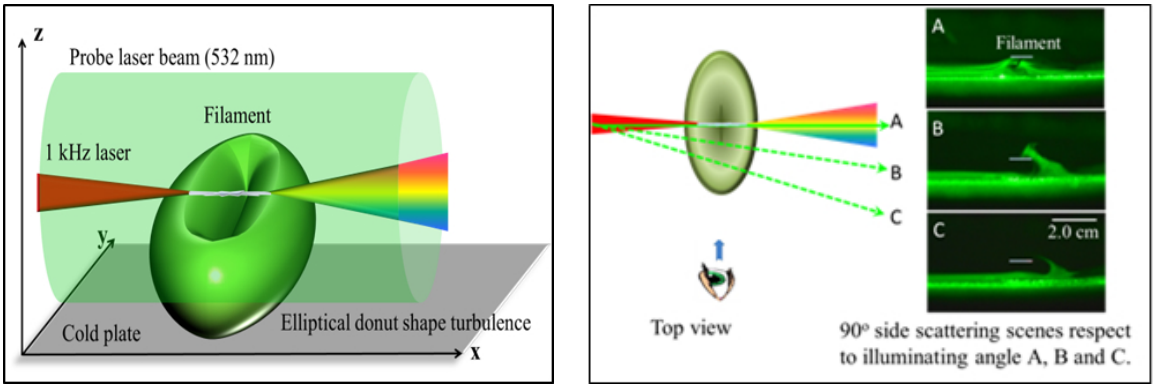

(a) **(b)**

Figure 5.9: (a) Three dimensional model of the laser-induced turbulence (laser propagation axis "x", cold plate surface "x-y") and **(b)** images of turbulence around filament taken for different probe laser illumination angles A, B, and C

waist size of vortex in angle C and the one in angle A is proof of this. In these images, the pattern is evidently not as perfect as the donut thought of based on the simulations. Most of the time, a single vortex alone could be seen on the right hand side. However, an occasional vortex would appear on the left hand side. There was a constant flow of air from the left to the right of the chamber, thanks to the laser windows. The suppression of the vortex on the left hand side is probably a direct consequence of this.

Based on the proposed elliptical donut-shaped model of turbulence, it could be possible to explain the peculiar shape and location of the snow pile. The results from the simulations in Figure 5.6 and Figure 5.7 show that the highest velocity is along the z-axis and is right at the centroid of the elliptical donut. The full grown droplets approach the peripheral area of the vortex tube and enter into collisions with other droplets in the centroid area as they are pushed out by centrifugal force. Such collisions would maximize the snow output below the filament. The collisional zone is longer along the major axis of the elliptical donut and thus the snow pile takes the shape of an ellipse with a major axis along the direction perpendicular to the filament.

To conclude this chapter, simulations and experiments show that condensation/precipitation inside the cloud chamber can be amplified with the right type of turbulence. The only shortcoming could be that experiments were carried out using a lens of 20 cm focal length alone, as it presented the strongest turbulence pattern. As a consequence, our understanding of condensation physics for lenses of longer focal lengths used in traditional and inverted chambers is elementary. Hence, there is immense scope for further research.

Conclusion

Condensation induced by femtosecond laser filaments is explored and presented in this dissertation. Experiments were conducted to understand the relationship between the laser filament and the production of water droplets and solid precipitation, under sub-saturated conditions. The results obtained from the experiments conducted at COPL were found to be in conflict with existing results. In sub-saturated conditions, condensation or solid precipitation is normally unexpected as it has not been observed. The results bear testimony to the fact that low saturation ratios do not hamper laser induced condensation/precipitation, provided the laser filament possesses the correct physical parameters such as repetition rate, energy, and the lens placed at the entrance of the chamber has an optimal focal length.

In order to confirm this, a chirped pulse amplified Ti-sapphire pulse working at a central wavelength of 800 nm, 1 kHz repetition rate and $\sim$2 mJ energy was used. The three sets of experiments that have been presented can be summarized as follows:

In the first experiment, an inverted glass chamber was used to confirm the presence of binary H_2O-HNO_3 clusters in a sub-saturated condition similar to the one found in nature ($\sim$60% R. H). A commercial cold plate is fitted on the top of the chamber to create the temperature gradient. A receptacle was placed under the filament inside the chamber to collect any existing precipitation. The interaction area was probed using a green laser (@532 nm) and the scattering was observed with and without a digital camera. Very small mist packets were observed along the laser axis, indicating that condensation occurred due to the laser filament. Moreover, ion chromatography was performed on the precipitate found inside

the receptacle. The results clearly showed traces of NO_3^- ions. Based on the observation of these ions, it was possible to ascertain that the laser chemistry pathways proposed by the Teramobile group in Europe held good in the sub-saturated condition as well.

In the second experiment, a similar setup was used to see if the filament could enhance condensation in sub-saturated conditions. To obtain optimal conditions for droplet growth, the conventional glass chamber was replaced by a smaller plexiglas chamber. Furthermore, a receptacle similar to the one in the first experiment was used to collect precipitation. In this experiment, it was cooled using a cold finger that was linked to the cold plate. The precipitation was studied without and with filament. The mass of precipitation found on the receptacle without the filament was subtracted from the mass found with the filament with a view to find the total growth in precipitation that was roughly $\sim$0.9 g. Thus, this confirmed our initial expectations of the filament being able to influence the mass of precipitation in sub-saturated conditions.To summarize the nature of the precipitation observed, it can be said that the condensation nuclei are generated in the filament area. They are then pushed into the super-saturated zone near the cold plate by thermally induced convection. These nuclei grow into larger droplets in this super-saturated zone and some of these droplets fall back into the receptacle while the others fall elsewhere in the chamber. To better understand how the laser filament-induced turbulence affects the condensation, a third experiment was performed.

In the third experiment, a systematic study was done for different focal lengths to comprehend how turbulence underwent modifications due to the lens placed at the entrance of the chamber. The setup had a traditional temperature gradient with the plate at the bottom. In addition, the manner in which this change in turbulence influences the condensation/precipitation in the chamber was also studied. The irradiation period for the laser filament was set to 60 minutes and four lenses of focal lengths 20, 30, 50 and 80 cm were tested. Digital camera pictures for each of these cases show different turbulence

patterns. The lenses having focal lengths of 20 and 30 cm gave rise to rapidly spinning vortices. In contrast, the 50 and 80 cm presented no vortices but a sliding mist packet alone. Distinguishable snow piles were collected below the filament on the surface of the cold plate. The lenses having focal lengths of 20 and 30 cm presented well resolved snow piles with significant masses ($\sim$12.5 and $\sim$5 mg). The snow piles exhibited peculiar characteristics. Firstly, they were elliptical in shape. Secondly, the major axis of the ellipse was perpendicular to filament when seen from above. Among the four lenses, the 20 cm lens presented the most active turbulence pattern with two clear vortices rotating at high angular velocities. Since the biggest elliptical snow pile was seen for this condition, this was probed further. The air current velocity at the edge of the vortices was estimated to be $\sim$16.5 cm/s. Simulation results show laser filament as a heat source can induce loops of turbulence both above and below the filament. Turbulence below the filament was found, experimentally and theoretically, to have an elliptical donut shape with a major axis perpendicular to the laser filament. The vortex offered a saturated or super-saturated environment inside which the injected Cloud Condensation Nuclei (CCN) such as HNO_3, N_2^+, O_2^+, as well as other ions and impurities could be activated. The multiple circumambulations inside the vortices provided the activated CCN ample time and possibility to grow in size by way of collisions with other water droplets/molecules. Once the particles reach a critical size, they are spun out from the vortices. With the constant feeding of moist air, delivered by the turbulence above the filament, the whole process repeats itself (saturation, super-saturation, and precipitation), thereby sustaining the precipitation mechanism. This model based on the elliptical donut-shaped turbulence explains the elliptical shape of the snow pile below the filament very well.

To conclude, we believe that the results of this dissertation can help to develop a better understanding of the underlying physical mechanisms of laser-induced condensation and precipitation in a sub-saturated environment. However, our understanding is far from complete and at best rudimentary. For example, in this work, a laser repetition of 1 kHz has

been used for all the experiments. The strength of the laser filament-turbulence was shown to be dependent on the laser repetition rate and the focal length of the lens placed at the entrance of the chamber. In future experiments, higher repetition rates could be explored to ensure that the complete potential of the laser filament-induced turbulence is unlocked. Not only can the CCN be spread to greater distances, but there is a chance for greater amplification in condensation/precipitation processes with the newly observed elliptical donut shaped turbulence. The eco-friendly use and implementation of turbulence induced by laser filament will be the real challenge and holds the key to a world of newer opportunities.

Appendix A

SolidWorks drawing of plexiglas chamber

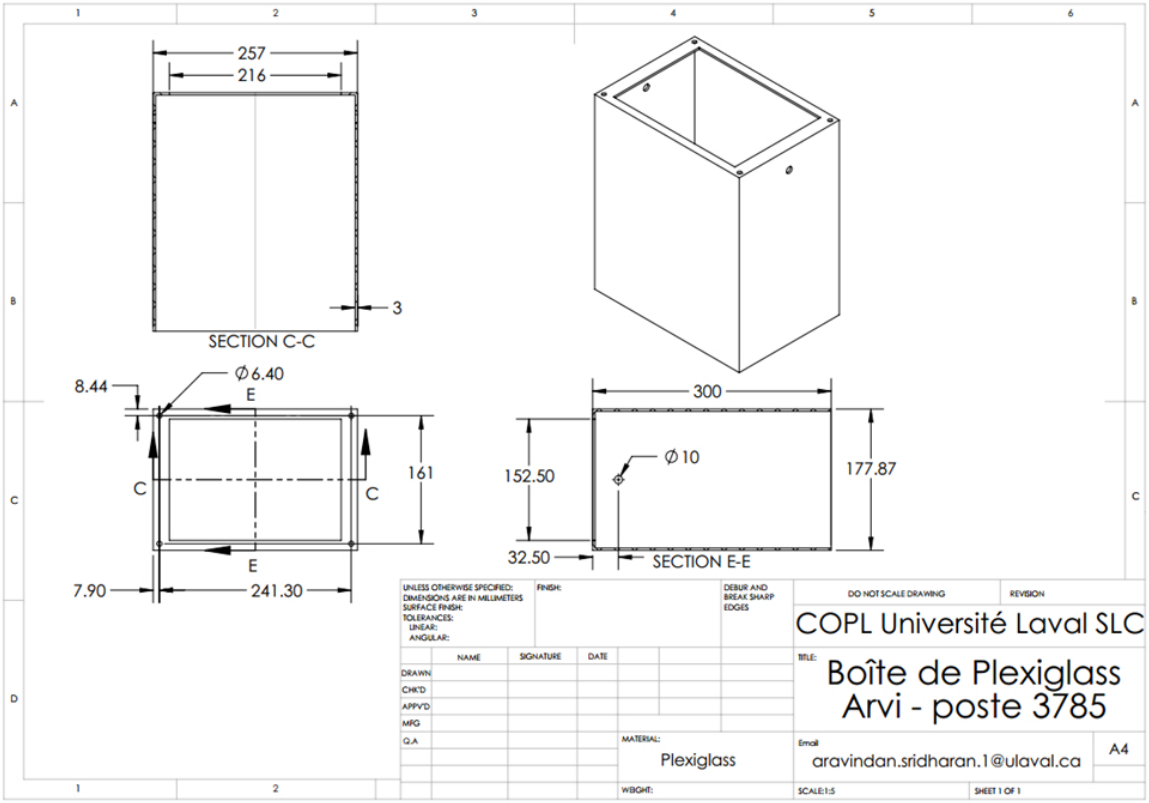

Figure A.1: SolidWorks drawing of the plexiglas chamber used in the droplet growth measurement setup described in Figure 4.1

Bibliography

[1] S. L. Chin, S. A. Hosseini, W. Liu, Q. Luo, F. Théberge, N. Aközbek, A. Becker, V. P. Kandidov, O. G. Kosareva, and H. Schroeder. The propagation of powerful femtosecond laser pulses in opticalmedia: physics, applications, and new challenges. *Canadian Journal of Physics*, 83(9):863–905, 2005. URL http://dx.doi.org/10.1139/p05-048.

[2] A. Couairon and A. Mysyrowicz. Femtosecond filamentation in transparent media. *Physics Reports*, 441(2–4):47–189, 2007. URL http://dx.doi.org/10.1016/j.physrep.2006.12.005.

[3] L. Bergé, S. Skupin, R. Nuter, J. Kasparian, and J.-P. Wolf. Ultrashort filaments of light in weakly ionized, optically transparent media. *Reports on Progress in Physics*, 70(10):1633, 2007. URL http://dx.doi.org/10.1088/0034-4885/70/10/R03.

[4] O. G. Kosareva, I. N. Murtazin, N. A. Panov, A. B. Savel'ev, V. P. Kandidov, and S. L. Chin. Pulse shortening due to filamentation in transparent medium. *Laser Physics Letters*, 4(2):126–132, 2007. URL http://dx.doi.org/10.1002/lapl.200610081.

[5] S.L. Chin, Y. Chen, O. Kosareva, V.P. Kandidov, and F. Théberge. What is a filament? *Laser Physics*, 18(8):962–964, 2008. URL http://dx.doi.org/10.1134/S1054660X08080070.

[6] J. Kasparian and J.-P. Wolf. Physics and applications of atmospheric nonlinear optics

and filamentation. *Optics Express*, 16(1):466–493, 2008. URL http://dx.doi.org/10.1364/OE.16.000466.

[7] V. P. Kandidov, S. A. Shlenov, and O. G. Kosareva. Filamentation of high-power femtosecond laser radiation. *Quantum Electronics*, 39(3):205, 2009. URL http://dx.doi.org/10.1070/QE2009v039n03ABEH013916.

[8] S. L. Chin. *Femtosecond Laser Filamentation*. Springer Series on Atomic, Optical, and Plasma Physics. University Science Books, 2010.

[9] S. L. Chin, T.-J. Wang, C. Marceau, J. Wu, J. S. Liu, O. Kosareva, N. Panov, Y. P. Chen, J.-F. Daigle, S. Yuan, A. Azarm, W. W. Liu, T. Seideman, H. P. Zeng, M. Richardson, R. Li, and Z. Z. Xu. Advances in intense femtosecond laser filamentation in air. *Laser Physics*, 22(1):1–53, 2012. URL http://dx.doi.org/10.1134/S1054660X11190054.

[10] Z. G. Ji, J. S. Liu, Z. X. Wang, J. Ju, X. M. Lu, Y. H. Jiang, Y. X. Leng, X. Y. Liang, W. Liu, S. L. Chin, R. X. Li, and Z. Z. Xu. Femtosecond laser filamentation with a 4 j/60 fs ti:sapphire laser beam: Multiple filaments and intensity clamping. *Laser Physics*, 20(4):886–890, 2010. URL http://dx.doi.org/10.1134/S1054660X10070145.

[11] S. Xu, J. Bernhardt, M. Sharifi, W. Liu, and S. L. Chin. Intensity clamping during laser filamentation by tw level femtosecond laser in air and argon. *Laser Physics*, 22(1):195–202, 2012. URL http://dx.doi.org/10.1134/S1054660X12010264.

[12] V. P. Kandidov, V. Yu. Fedorov, O. V. Tverskoi, O. G. Kosareva, and S. L. Chin. Intensity clamping in the filament of femtosecond laser radiation. *Quantum Electronics*, 41(4):382, 2011. URL http://dx.doi.org/10.1070/QE2011v041n04ABEH014486.

[13] A. Braun, G. Korn, X. Liu, D. Du, J. Squier, and G. Mourou. Self-channeling of high-peak-power femtosecond laser pulses in air. *Optics Letters*, 20(1):73–75, 1995. URL http://dx.doi.org/10.1364/OL.20.000073.

[14] R. W. Boyd. *Nonlinear Optics*. Academic Press, 3rd edition, 2008.

[15] J. H. Marburger. Self-focusing: Theory. *Progress in Quantum Electronics*, 4:35–110, 1975. URL http://dx.doi.org/10.1016/0079-6727(75)90003-8.

[16] G. Fibich and A. L. Gaeta. Critical power for self-focusing in bulk media and in hollow waveguides. *Optics Letters*, 25(5):335–337, 2000. URL http://dx.doi.org/10.1364/OL.25.000335.

[17] W. Liu and S. L. Chin. Direct measurement of the critical power of femtosecond ti:sapphire laser pulse in air. *Optics Express*, 13(15):5750–5755, 2005. URL http://dx.doi.org/10.1364/OPEX.13.005750.

[18] L. V. Keldysh. Ionization in the field of a strong electromagnetic wave. *Journal of Experimental and Theoretical Physics*, 20(5):1307–1314, 1965. URL http://jetp.ac.ru/cgi-bin/dn/e_020_05_1307.pdf.

[19] S. L. Chin. From multiphoton to tunnel ionization. In Y. Fujimura A. A. Villaeys and S. H. Lin, editors, *Advances in Multiphoton Processes and Spectroscopy*, volume 16, pages 249–272. World Scientific, 2004.

[20] L. Bergé. Wave collapse in physics: principles and applications to light and plasma waves. *Physics Reports*, 303(5–6):259–370, 1998. URL http://dx.doi.org/10.1016/S0370-1573(97)00092-6.

[21] O. G. Kosareva, N. A. Panov, D. S. Uryupina, M. V. Kurilova, A. V. Mazhorova, A. B. Savel'ev, R. V. Volkov, V. P. Kandidov, and S. L. Chin. Optimization of a femtosecond pulse self-compression region along a filament in air. *Applied Physics B*, 91(1):35–43, 2008. URL http://dx.doi.org/10.1007/s00340-008-2959-9.

[22] W. L. Kruer. *The Physics of Laser Plasma Interactions*. Addison-Wesley, Redwood City, 1st edition, 1988.

[23] A. Brodeur, C. Y. Chien, F. A. Ilkov, S. L. Chin, O. G. Kosareva, and V. P. Kandidov. Moving focus in the propagation of ultrashort laser pulses in air. *Optics Letters*, 22(5): 304–306, 1997. URL http://dx.doi.org/10.1364/OL.22.000304.

[24] E. T. J. Nibbering, P. F. Curley, G. Grillon, B. S. Prade, M. A. Franco, F. Salin, and A. Mysyrowicz. Conical emission from self-guided femtosecond pulses in air. *Optics Letters*, 21(1):62–64, 1996. URL http://dx.doi.org/10.1364/OL.21.000062.

[25] M. Mlejnek, E. Wright, and J. Moloney. Power dependence of dynamic spatial replenishment of femtosecond pulses propagating in air. *Optics Express*, 4(7):223–228, 1999. URL http://dx.doi.org/10.1364/OE.4.000223.

[26] A. Couairon. Light bullets from femtosecond filamentation. *The European Physical Journal D - Atomic, Molecular, Optical and Plasma Physics*, 27(2):159–167, 2003. URL http://dx.doi.org/10.1140/epjd/e2003-00255-9.

[27] M. Rodriguez, R. Bourayou, G. Méjean, J. Kasparian, J. Yu, E. Salmon, A. Scholz, B. Stecklum, J. Eislöffel, U. Laux, A. P. Hatzes, R. Sauerbrey, L. Wöste, and J.-P. Wolf. Kilometer-range nonlinear propagation of femtosecond laser pulses. *Physical Review E*, 69:036607, 2004. URL http://dx.doi.org/10.1103/PhysRevE.69.036607.

[28] J. Kasparian, M. Rodriguez, G. Méjean, J. Yu, E. Salmon, H. Wille, R. Bourayou, S. Frey, Y.-B. André, A. Mysyrowicz, R. Sauerbrey, J.-P. Wolf, and L. Wöste. White-light filaments for atmospheric analysis. *Science*, 301(5629):61–64, 2003. URL http://dx.doi.org/10.1126/science.1085020.

[29] H. L. Xu, Y. Kamali, C. Marceau, P. T. Simard, W. Liu, J. Bernhardt, G. Mejean, P. Mathieu, G. Roy, J.-R. Simard, and S. L. Chin. Simultaneous detection and identification of multigas pollutants using filament-induced nonlinear spectroscopy. *Applied Physics Letters*, 90(10):101106, 2007. URL http://dx.doi.org/10.1063/1.2711537.

[30] J.-F. Daigle, G. Méjean, W. Liu, F. Théberge, H. L. Xu, Y. Kamali, J. Bernhardt, A. Azarm, Q. Sun, P. Mathieu, G. Roy, J.-R. Simard, and S. L. Chin. Long range trace detection in aqueous aerosol using remote filament-induced breakdown spectroscopy. *Applied Physics B*, 87(4):749–754, 2007. URL http://dx.doi.org/10.1007/s00340-007-2642-6.

[31] H. L. Xu, G. Méjean, W. Liu, Y. Kamali, J.-F. Daigle, A. Azarm, P. T. Simard, P. Mathieu, G. Roy, J.-R. Simard, and S. L. Chin. Remote detection of similar biological materials using femtosecond filament-induced breakdown spectroscopy. *Applied Physics B*, 87(1):151–156, 2007. URL http://dx.doi.org/10.1007/s00340-006-2536-z.

[32] S. L. Chin, H. L. Xu, Q. Luo, F. Théberge, W. Liu, J.-F. Daigle, Y. Kamali, P. T. Simard, J. Bernhardt, S. A. Hosseini, M. Sharifi, G. Méjean, A. Azarm, C. Marceau, O. Kosareva, V. P. Kandidov, N. Aközbek, A. Becker, G. Roy, P. Mathieu, J. R. Simard, M. Châteauneuf, and J. Dubois. Filamentation "remote" sensing of chemical and biological agents/pollutants using only one femtosecond laser source. *Applied Physics B*, 95(1):1–12, 2009. URL http://dx.doi.org/10.1007/s00340-009-3381-7.

[33] N. Khan, N. Mariun, I. Aris, and J. Yeak. Laser-triggered lightning discharge. *New Journal of Physics*, 4(1):61, 2002. URL http://dx.doi.org/10.1088/1367-2630/4/1/361.

[34] M. Rodriguez, R. Sauerbrey, H. Wille, L. Wöste, T. Fujii, Y.-B. André, A. Mysyrowicz, L. Klingbeil, K. Rethmeier, W. Kalkner, J. Kasparian, E. Salmon, J. Yu, and J.-P. Wolf. Triggering and guiding megavolt discharges by use of laser-induced ionized filaments. *Optics Letters*, 27(9):772–774, 2002. URL http://dx.doi.org/10.1364/OL.27.000772.

[35] H. Pépin, D. Comtois, F. Vidal, C. Y. Chien, A. Desparois, T. W. Johnston, J. C.

Kieffer, B. La Fontaine, F. Martin, F. A. M. Rizk, C. Potvin, P. Couture, H. P. Mercure, A. Bondiou-Clergerie, P. Lalande, and I. Gallimberti. Triggering and guiding high-voltage large-scale leader discharges with sub-joule ultrashort laser pulses. *Physics of Plasmas (1994-present)*, 8(5):2532–2539, 2001. URL http://dx.doi.org/10.1063/1.1342230.

[36] D. J. Cook and R. M. Hochstrasser. Intense terahertz pulses by four-wave rectification in air. *Optics Letters*, 25(16):1210–1212, 2000. URL http://dx.doi.org/10.1364/OL.25.001210.

[37] C. D. Amico, A. Houard, S. Akturk, Y. Liu, J. Le Bloas, M. Franco, B. Prade, A. Couairon, V. T. Tikhonchuk, and A. Mysyrowicz. Forward THz radiation emission by femtosecond filamentation in gases: theory and experiment. *New Journal of Physics*, 10(1):013015, 2008. URL http://dx.doi.org/10.1088/1367-2630/10/1/013015.

[38] T.-J. Wang, Y. Chen, C. Marceau, F. Théberge, M. Châteauneuf, J. Dubois, and S. L. Chin. High energy terahertz emission from two-color laser-induced filamentation in air with pump pulse duration control. *Applied Physics Letters*, 95(13):131108, 2009. URL http://dx.doi.org/10.1063/1.3242024.

[39] Y. Zhang, Y. Chen, S. Xu, H. Lian, M. Wang, W. Liu, S. L. Chin, and G. Mu. Portraying polarization state of terahertz pulse generated by a two-color laser field in air. *Optics Letters*, 34(18):2841–2843, 2009. URL http://dx.doi.org/10.1364/OL.34.002841.

[40] T.-J. Wang, C. Marceau, Y. Chen, S. Yuan, F. Théberge, M. Châteauneuf, J. Dubois, and S. L. Chin. Terahertz emission from a dc-biased two-color femtosecond laser-induced filament in air. *Applied Physics Letters*, 96(21):211113, 2010. URL http://dx.doi.org/10.1063/1.3441004.

[41] H. R. Pruppacher and J. D. Klett. *Microphysics of Clouds and Precipitation*. Kluwer Academic Publishing, 1997.

[42] H. Kohler. The nucleus in and the growth of hygroscopic droplets. *Transactions of the Faraday Society*, 32:1152–1161, 1936. URL http://dx.doi.org/10.1039/TF9363201152.

[43] J. Qiu and D. Cressey. Meteorology: Taming the sky. *Nature*, 453:970–974, 2008. URL http://dx.doi.org/10.1038/453970a.

[44] K. Yoshihara. Laser-induced mist and particle formation from ambient air: A possible new cloud seeding method. *Chemistry Letters*, 34:1370–1371, 2005. URL http://dx.doi.org/10.1246/cl.2005.1370.

[45] K. Yoshihara, Y. Takatori, K. Miyazaki, and Y. Kajii. Ultraviolet light-induced water-droplet formation from wet ambient air. *Proceedings of the Japan Academy, Series B*, 83(9+10):320–325, 2007. URL http://dx.doi.org/10.2183/pjab.83.320.

[46] P. Rohwetter, J. Kasparian, K. Stelmaszczyk, Z. Hao, S. Henin, N. Lascoux, W. M. Nakaema, Y. Petit, M. Queißer, R. Salamé, E. Salmon, L. Wöste, and J.-P. Wolf. Laser-induced water condensation in air. *Nature Photonics*, 4:451–456, 2010. URL http://dx.doi.org/10.1038/nphoton.2010.115.

[47] J. Kasparian, L. Wöste, and J.-P. Wolf. Laser-based weather control. *Optics and Photonics News*, 21:22–27, 2010. URL http://www.osa-opn.org/home/articles/volume_21/issue_7/features/laser-based_weather_control/#.Uo_h9NJDtDm.

[48] Y. Petit, S. Henin, J. Kasparian, and J.-P. Wolf. Production of ozone and nitrogen oxides by laser filamentation. *Applied Physics Letters*, 97(2):021108, 2010. URL http://dx.doi.org/10.1063/1.3462937.

[49] Y. Petit, S. Henin, J. Kasparian, J. P. Wolf, P. Rohwetter, K. Stelmaszczyk, Z. Q. Hao, W. M. Nakaema, L. Wöste, A. Vogel, T. Pohl, and K. Weber. Influence of pulse duration, energy, and focusing on laser-assisted water condensation. *Applied Physics Letters*, 98 (4):041105, 2011. URL http://dx.doi.org/10.1063/1.3546172.

[50] S. Henin, Y. Petit, P. Rohwetter, K. Stelmaszczyk, Z. Q. Hao, W. M. Nakaema, A. Vogel, T. Pohl, F. Schneider, J. Kasparian, K. Weber, L. Wöste, and J.-P. Wolf. Field measurements suggest the mechanism of laser-assisted water condensation. *Nature Communications*, 2:456, 2011. URL http://dx.doi.org/10.1038/ncomms1462.

[51] P. Rohwetter, J. Kasparian, L. Wöste, and J.-P. Wolf. Modelling of HNO_3-mediated laser-induced condensation: A parametric study. *The Journal of Chemical Physics*, 135 (13):134703, 2011. URL http://dx.doi.org/10.1063/1.3644591.

[52] H. Saathoff, S. Henin, K. Stelmaszczyk, M. Petrarca, R. Delagrange, Z. Hao, J. Lüder, O. Möhler, Y. Petit, P. Rohwetter, M. Schnaiter, J. Kasparian, T. Leisner, J.-P. Wolf, and L. Wöste. Laser filament-induced aerosol formation. *Atmospheric Chemistry and Physics*, 13(9):4593–4604, 2013. URL http://dx.doi.org/10.5194/acp-13-4593-2013.

[53] Thomas Leisner, Denis Duft, Ottmar Möhler, Harald Saathoff, Martin Schnaiter, Stefano Henin, Kamil Stelmaszczyk, Massimo Petrarca, Raphaëlle Delagrange, Zuoqiang Hao, Johannes Lüder, Yannick Petit, Philipp Rohwetter, Jérôme Kasparian, Jean-Pierre Wolf, and Ludger Wöste. Laser-induced plasma cloud interaction and ice multiplication under cirrus cloud conditions. *Proceedings of the National Academy of Sciences*, 110(25):10106–10110, 2013. URL http://dx.doi.org/10.1073/pnas.1222190110.

[54] A. Langsdorf. A continuously sensitive diffusion cloud chamber. *Review of Scientific Instruments*, 10(3):91–103, 1939. URL http://dx.doi.org/10.1063/1.1751494.

[55] I. Saavedra. On the theory of the diffusion cloud chamber. *Nuclear Instruments*, 3(2): 85–89, 1958. URL http://dx.doi.org/10.1016/0369-643X(58)90096-3.

[56] J. L. Katz and P. Mirabel. Calculation of supersaturation profiles in thermal diffusion cloud chambers. *Journal of the Atmospheric Sciences*, 32:646–652, 1975. URL http://dx.doi.org/10.1175/1520-0469(1975)032<0646:COSPIT>2.0.CO;2.

[57] J. Ju, J. Liu, C. Wang, H. Sun, W. Wang, X. Ge, C. Li, S. L. Chin, R. Li, and Z. Xu. Laser-filamentation-induced condensation and snow formation in a cloud chamber. *Optics Letters*, 37(7):1214–1216, 2012. URL http://dx.doi.org/10.1364/OL.37.001214.

[58] J. Ju, J. Liu, C. Wang, H. Sun, W. Wang, X. Ge, C. Li, S. L. Chin, R. Li, and Z. Xu. Effects of initial humidity and temperature on laser-filamentation-induced condensation and snow formation. *Applied Physics B*, 110(3):375–380, 2013. URL http://dx.doi.org/10.1007/s00340-012-5265-5.

[59] H. Sun, J. Liu, C. Wang, J. Ju, Z. Wang, W. Wang, X. Ge, C. Li, S. L. Chin, R. Li, and Z. Xu. Laser filamentation induced air-flow motion in a diffusion cloud chamber. *Optics Express*, 21(8):9255–9266, 2013. URL http://dx.doi.org/10.1364/OE.21.009255.

[60] R. A. Shaw. Supersaturation intermittency in turbulent clouds. *Journal of the Atmospheric Sciences*, 57:3452–3456, 2000. URL http://dx.doi.org/10.1175/1520-0469(2000)057<3452:SIITC>2.0.CO;2.